

Inorganic CsPbI₂Br Perovskite Solar Cells: The Progress and Perspective

Qingsen Zeng, Xiaoyu Zhang, Chongming Liu, Tanglue Feng, Zhaolai Chen, Wei Zhang, Weitao Zheng, Hao Zhang, and Bai Yang*

Cesium-based all-inorganic perovskite solar cells (PSCs), especially for CsPbI₂Br component-based devices, have attracted increasing attention due to its advantage of superior thermal and phase stability. Since the pioneering study reported in 2016, more than 30 papers have been published, reporting the rapid boost in the power conversion efficiency (PCE) of PSCs to 14.81%. The CsPbI₂Br PSC is one of the most remarkable research hotspots in the field of perovskite photovoltaics. In this progress report, the recent advances in CsPbI₂Br PSCs are systematically reviewed, which in turn introduces the basic property and stability of active layers, and the performance improvements in these devices. The challenges as well as the possible solutions toward better-performing CsPbI₂Br PSCs are also discussed. The theoretical calculation results point out that there is much room for further device performance enhancement, particularly in open-circuit voltages. This progress report focuses on CsPbI₂Br material properties and summarizes recent strategies to improve the corresponding device's PCE, in order to open new perspectives toward commercial utility of PSCs.

1. Introduction

The lead halide perovskite materials have been under the spotlight owing to the excellent optical and electrical properties, such as high absorption coefficient,^[1] low exciton binding energy,^[2] ultralong charge carrier diffusion length,^[3] and superhigh defect tolerance with low trap state density.^[4] The power conversion efficiency (PCE) of perovskite solar cells (PSCs) now stands at 23.3%,^[5] starting from 3.8% as reported by Miyasaka et al. in 2009.^[6] Although the PCEs of organic-inorganic hybrid PSCs are comparable to those of commercial solar cells, their instability hampers their further commercialization.^[7] As an alternative, cesium-based all-inorganic perovskites show better light, moisture and especially thermal stability, providing a possible path to stable PSCs.^[8]

In inorganic Pb-halide perovskites, the cubic (α) CsPbI₃ with a band gap (E_g) of 1.73 eV is the best fit for photovoltaic application. Unfortunately, bulk CsPbI₃ is only stable in the cubic perovskite phase at high temperature, and rapidly converts to non-perovskite orthorhombic (δ) phase ($E_g = 2.82$ eV) with poor photoelectric properties at room temperature in moisture atmosphere. The preliminary attempt has shown a PCE of 0.09% based on the non-perovskite CsPbI₃.^[9] Suffering from the poor phase stability, the all-inorganic PSCs developed late, but progressed fast in the last 2 years. Until 2015, the genuine inorganic CsPbI₃ PSCs with a PCE of 2.9% was demonstrated first by Snaith et al. through reducing grain size with the aid of hydriodic acid (HI).^[10] The next year, Luther et al. published a significant paper in *Science*.^[11] They demonstrate that the phase transition temperature of CsPbI₃ quantum dots (QDs) is far below that of the bulk materials. The CsPbI₃ QDs maintain their α -phase for months at room temperature in ambient air. Air-stable and efficient α -CsPbI₃ QD solar cells with the PCE of over 10% have been obtained. Since then, various methods including ion doping,^[12] small molecular or polymer modification,^[13] and dimension control^[14] have been developed rapidly to stabilize the cubic phase of CsPbI₃ via reducing grain size. The passivation of grain boundaries or surface states becomes critical for high-efficiency CsPbI₃ PSCs, because of the fact that there will be more grain boundaries and thus more surface states as the crystal size decreases.^[15]

Q. Zeng, C. Liu, T. Feng, Prof. H. Zhang, Prof. B. Yang
State Key Laboratory of Supramolecular Structure and Materials
College of Chemistry
Jilin University
Changchun 130012, P. R. China
E-mail: byangchem@jlu.edu.cn

Dr. X. Zhang, Prof. W. Zhang, Prof. W. Zheng
Department of Materials Science
Key Laboratory of Mobile Materials MOE
State Key Laboratory of Automotive Simulation and Control
Jilin University
Changchun 130012, P. R. China

Dr. Z. Chen
Division of Physical Sciences and Engineering
Solar and Photovoltaics Engineering Research Center (SPERC)
King Abdullah University of Science and Technology (KAUST)
Thuwal 23955-6900, Kingdom of Saudi Arabia

Prof. B. Yang
State Key Laboratory of Applied Optics
Changchun Institute of Optics
Fine Mechanics and Physics
Chinese Academy of Sciences
Changchun 130033, P. R. China

DOI: 10.1002/solr.201800239

In 2016, Snaith et al. demonstrated that the cesium lead mixed-halide perovskites, CsPbI₂Br, are stable in the cubic phase at room temperature even for bulk materials.^[16] The CsPbI₂Br exhibits reasonable bandgaps of 1.82–1.92 eV depending on the deposition method, showing great potential in tandem and semitransparent photovoltaic applications. The enhanced phase stability of CsPbI₂Br thin film is owing to the increased effective tolerance factor and lowered phase transition temperature. The first CsPbI₂Br solar cell has shown a surprisingly PCE of 9.8%.^[16] Recently, the PCE of CsPbI₂Br PSCs has been rapidly promoted to 14.8% as a result of crystal morphology control, grain boundary passivation, interface engineering, and device structure optimization.^[17] Although the device stability of inorganic CsPbI₂Br PSCs is significantly better than that of the hybrid component, but their PCEs still lag behind that of the hybrid perovskite devices. More efforts should be paid on energy level matching, doping density optimizing, and charge transport and collection improvement for high performance CsPbI₂Br PSCs with maximized short-circuit current (J_{sc}) and minimized energy loss (E_{loss}).

In this *Progress Reports*, we begin with a discussion of electronic and optical properties of CsPbI₂Br perovskites. We proceed to review briefly the thermal-, phase-, and light-stability of CsPbI₂Br perovskites and solar cell operational stability. We then introduce the strategies to improve the performance of CsPbI₂Br PSCs, including the crystallization control, defect passivation, and interface engineering. We follow with a theoretical calculation of the PCE limit of CsPbI₂Br PSCs, revealing that there is still much room for device performance improvement. We close with a perspective on challenges and opportunities remaining open in the field.

2. Materials Properties

Theoretical calculations indicate that there is no difference in electronic and optical properties between all-inorganic and organic-inorganic hybrid perovskites, when the organic moiety are replaced with inorganic Cs⁺ cations.^[18] However, only limited electronic and optical experimental results have been reported for the bulk Cs-based perovskites. Nicholas et al. first systematically studied the basic properties of CsPbI₂Br, including the exciton binding energy (R^*), reduced mass (μ), the presence of phase transition, and the dielectric screening.^[19] The temperature-dependent transmission spectra of CsPbI₂Br were measured over a wide range of temperatures from 4.2 to 270 K (Figure 1a). It's worth noting that no new peaks appear when increasing the temperatures, while the single peak broadens and blue-shifts. The band gaps present a well-behaved monotonic dependence upon the temperatures, which indicates that the CsPbI₂Br preserves the photoactive cubic perovskite phase even at cryogenic temperatures. This contrasts sharply with the hybrid perovskites, where the band gap increases at temperatures corresponding to the phase transitions to a lower-symmetry crystalline structure.^[20] The excellent phase stability against cryogenic temperature of CsPbI₂Br perovskites is inspiring and is the base for producing stable PSCs.

Next, the exciton binding energy and reduced mass have been precisely determined from the low-temperature magneto-



Qingsen Zeng is a PhD student at the State Key Lab of Supramolecular Structure and Materials under the supervision of Prof. Bai Yang, majoring in polymer chemistry and physics. He is interested in organic polymer- and inorganic nanocrystal-based photoelectronic materials, and now focuses on exploring new procedures to synthesize stable

CsPbX₃ perovskites nanocrystals and optimizing their performance in polymer-based hybrid solar cells.



Xiaoyu Zhang studied device physics at Jilin University in China, where he received his PhD in 2016. In the same year, he joined the College of Materials Science and Engineering, Jilin University, as a postdoctoral fellow to research quantum dot solar cells and light-emitting diodes. His research interests include the development of green and efficient

nanomaterials and to understand their semiconductor property relations for energy and light-emitting applications.



Bai Yang is currently a professor of chemistry at the State Key Lab of Supramolecular Structure and Materials in the College of Chemistry, Jilin University. He received his PhD in polymer physics and chemistry in 1991 under the supervision of Prof. Jiacong Shen at Jilin University. His current research interests include carbon-based

nanodots (carbonized polymer dots and graphene quantum dots), polymer/nanocrystals based high-performance optical and photoelectric materials, and multi-scale ordered polymeric microstructures for photonic responsive materials.

transmission spectroscopy. The energetic minima in absorption spectra was plotted as a function of the magnetic field (Figure 1b). The exciton binding energy (22 ± 3 meV) and reduced mass ($0.124 \pm 0.02 m_0$) have been extracted from analyzing of the full magnetic field dependence on both hydrogenic and free carrier transitions. The exciton binding energy of CsPbI₂Br is slightly larger than that of MAPbI₃ (16 meV) and CsPbI₃ (15 ± 1 meV) perovskites,^[20–21] but the excitons in CsPbI₂Br perovskites can still dissociate into free carriers at room temperature. The effective dielectric constant ϵ_{eff} of 8.6 has also been determined from the exciton binding energy and reduced effective mass.

Furthermore, the transport and relaxation dynamics in individual CsPbI₂Br crystals has been investigated using the

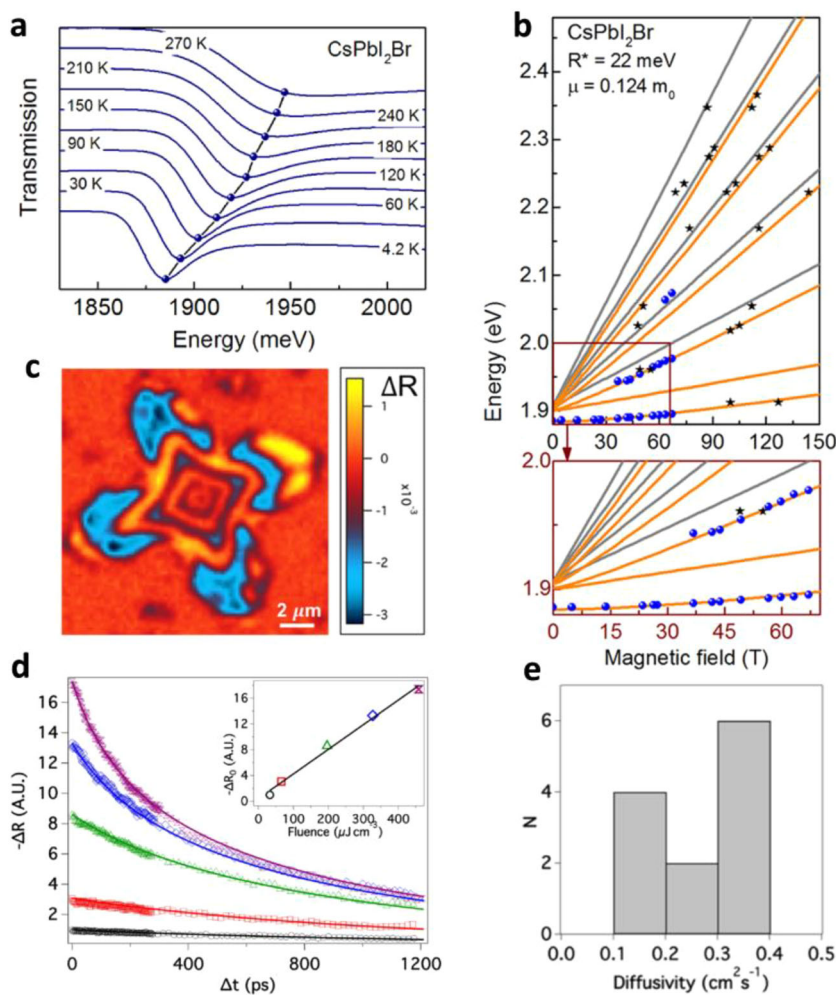


Figure 1. a) Temperature-dependent transmission for CsPbI₂Br. The evolution of the absorption peak with temperature is highlighted by symbols. b) Excitonic transition and inter-Landau level transition energies as a function of magnetic field at 2 K for CsPbI₂Br. Orange lines indicate fitting results of the hydrogen-like transitions. Gray lines are fitting results of the inter band transition between Landau levels. Circles and stars are data from long pulse field and single-turn short pulse measurements, respectively. An expanded view of the low-field and low-energy portion of the fan chart are given in the lower panels. Reproduced with permission.^[19] Copyright 2017, American Chemical Society. c) Transient reflectivity image for CsPbI₂Br perovskite domain collected at a pump–probe delay of 0 ps. d) Power-dependent transient reflectivity kinetics of a single CsPbI₂Br domain. The inset shows that $-\Delta R$ at $\Delta t = 0$ ps scales linearly with pump fluence. e) Histogram of diffusion constants measured for 12 individual domains. Reproduced with permission.^[21] Copyright 2017, American Chemical Society.

pump–probe microscopy by Grumstrup and coworkers.^[22] The transient reflectivity (TR) images were obtained via scanning the domain beneath spatially and temporally overlapped pump and probe beams (Figure 1c). The TR response can discriminate between the equilibrium and photoexcited mode position, thus giving a sensitive probe of the excited-state dynamics. Through fitting the power-dependent decay kinetics collected from five individual CsPbI₂Br domains (Figure 1d), the excited-state has been found to decay mainly via first-order (trap-assisted) and Auger recombination, with negligible second-order (bimolecular) recombination. This differs substantially from the dominant

recombination mechanism of the hybrid MAPbI₃ perovskites, which primarily exhibits second-order kinetics in the absence of trap-assisted recombination.^[23] The diffusion constant (D_c) of CsPbI₂Br has been determined ranging between 0.13 and 0.39 cm² s⁻¹ from the spatially separated pump-probe microscopy (Figure 1e). The diffusivity is related to the more commonly referenced ambipolar charge carrier mobility ($\mu_A = 5\text{--}15\text{--cm}^2\text{Vs}^{-1}$) through the Einstein relation ($\mu_A = D_c q/kT$, where q is the elementary charge, k the Boltzmann constant, and T is the temperature). The value is significantly lower than the mobility of MAPbI₃ (28–68 cm² Vs⁻¹).^[23] The reducing in mobility of CsPbI₂Br in comparison with hybrid MAPbI₃ perovskites is dominant by the higher trap density.^[21] Therefore, passivation of the trap states is essentially vital to enhance the charge carrier mobilities of CsPbI₂Br films and thus to obtain PSCs with higher-performances. Note that the orthorhombic CsPbI₂Br perovskite was used in this work,^[21] whose semiconductor properties are poorer than that of cubic CsPbI₂Br, which has been typically used in PSCs. The effect of crystal phase on charge carrier transport and recombination properties is still waiting for deeply exploring.

3. Materials Stability

Stable perovskites are critical to achieve highly durable PSCs toward their commercial utility. The organic-inorganic hybrid perovskite semiconductor decomposes rapidly when exposing to prolonged heat, moist air, or illuminations. By contrast, the all-inorganic perovskite materials have shown better stability under environmental stress.

3.1. Thermal Stability

For commercial photovoltaic modules have to be able to work successfully at over 85 °C, and in some geographic locations with high solar irradiance such high operating temperature can be regularly reached.^[16] This reality calls for the active layers to be composition stable under thermal stress. The thermal stability of CsPbI₂Br in ambient atmosphere has been investigated firstly by Snaith et al.^[16] The CsPbI₂Br thin film annealed at 350 °C shows optimal crystallinity and absorbance, and bears sintered temperature up to 400 °C. In contrast, both MA- and FA-based organic–inorganic hybrid perovskites decompose rapidly at such high temperatures. Specifically, the thermally degrade temperatures for MAPbI₃ and FAPbI₃ thin films are above 85 and 150 °C, respectively. The comparison of thermal and

atmospheric durability between CsPbI₂Br and MAPbI₂Br further demonstrates that CsPbI₂Br has better stability. **Figure 2** shows the absorption and XRD spectra of CsPbI₂Br and MAPbI₂Br films heated at 85 °C in 20–25% relative humidity (RH) over time. For CsPbI₂Br, the absorption spectra keep almost constant within 270 min. The absorbance at 627 nm does not decrease at all (insert of Figure 2a). As presented in Figure 2c, no peak indicates degradation or new composition as observed in the XRD patterns of the CsPbI₂Br perovskites before and after annealing. In contrast, the absorbance at 670 nm decreases continuously over 270 min for MAPbI₂Br (Figure 2b). Figure 2d shows the XRD patterns of MAPbI₂Br before and after annealing. The emerging of new peaks obviously reveals the decomposition product of PbI_{2-x}Br_x after annealing, with the volatilization of MABr and MAI. Therefore, it is concluded that the CsPbI₂Br exhibits both excellent structure and compositional stability against moisture and heat. The improved material thermal stability significantly promotes the CsPbI₂Br device stability, as have been demonstrated by many groups.^[17b,24]

3.2. Phase Stability

In spite the CsPbI₂Br has shown enhanced phase stability compares to that of neat CsPbI₃, it still suffers from phase transition to the non-perovskite phase when exposes to strong

moisture in ambient atmosphere, even though it can reversibly convert to cubic perovskite phase with the aid of annealing. The moisture induced phase transition mechanism was investigated and found to be fundamentally different from the hydration/dehydration process of hybrid MAPbI₃. The Moisture adsorbed on the CsPbI₂Br surface can introduce vacancies to the crystal lattice and lower the nucleation free-energy barrier, which catalyzes the perovskite to non-perovskite phase transition,^[25] while water molecules penetrate the crystal lattice and then is followed by multistep hydration before total decomposition of MAPbI₃.^[26] The thermochromic devices have been fabricated utilizing the reversible structural phase transitions.^[25] However, phase instability harms the device operational stability. Essentially, the phase instability is mainly caused by the too small Cs⁺ size in holding the [PbX₆]⁴⁻ (X = Br, I) octahedra. The effective tolerance factor (t_{eff}) of CsPbI₂Br (0.855) is slightly larger than that of CsPbI₃ (0.847), but still far away from the values between 0.9 and 1.0 for stable perovskite phase.^[7b] Yin et al. introduce fluorine (F) into CsPbI₂Br to promote the phase stability due to the improved t_{eff} .^[27] Correspondingly, devices based on the optimized composition of CsPbBrI_{1.78}F_{0.22} present enhanced stability and achieve an improved PCE of 10.26%. Yang et al. obtain stable inorganic perovskite films in humid ambient atmosphere through partly replacing Pb with germanium (Ge), whose ion radius (73 Å) is much smaller than that of Pb ion (119 Å), thus leading to enhanced t_{eff} . The CsPb_{0.8}Ge_{0.2}I₂Br PSC shows a

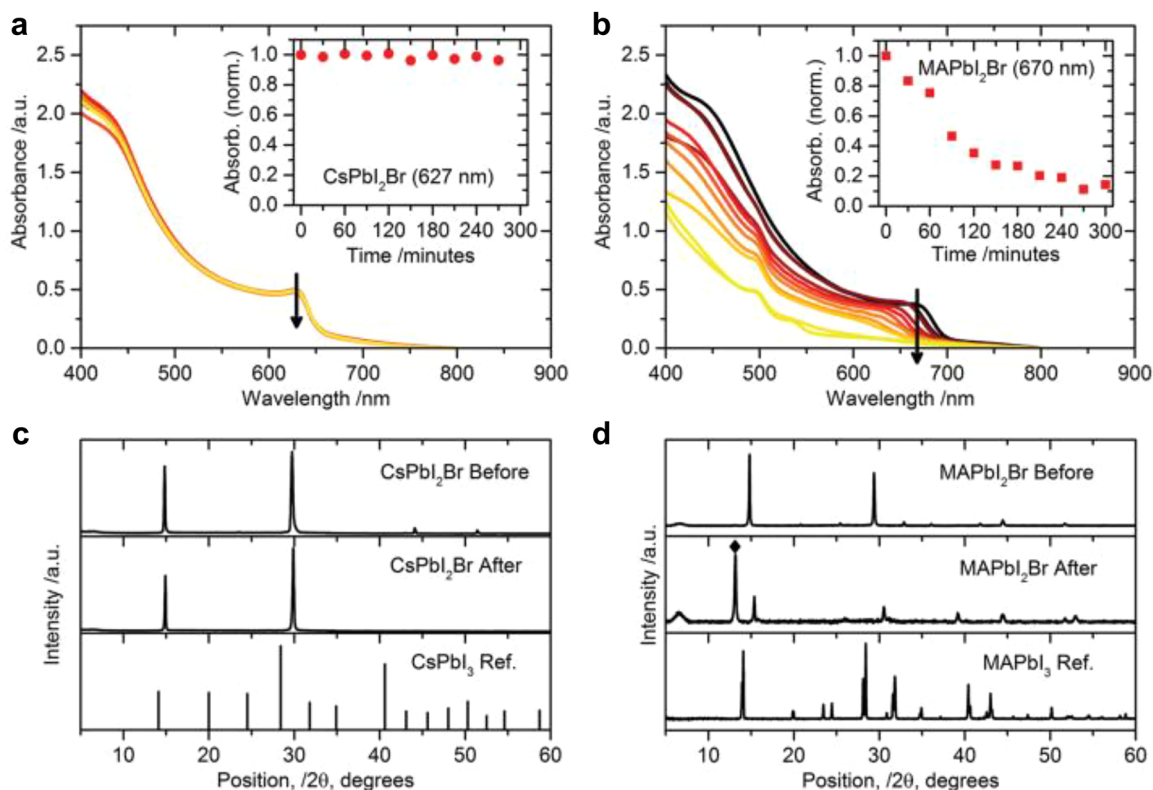


Figure 2. a) CsPbI₂Br and (b) MAPbI₂Br film absorption over time at 85 °C in 20–25% RH. The arrow orientation stands for increasing the heating time. Insets: absorption intensity change over time. XRD patterns for (c) CsPbI₂Br and (d) MAPbI₂Br before and after 85 °C heating for 270 min in 20–25% RH. The diamond represents for the peak position of PbI_{2-x}Br_x. Reproduced with permission.^[16] Copyright 2016, Wiley-VCH.

champion PCE of 10.8% with high V_{oc} of 1.27 V, and presents excellent performance stability in 50–60% relative humidity without encapsulation.^[24c] In addition, Han and coworkers demonstrate that $Pb(CH_3COO)_2$ additive can effectively stabilize the cubic phase through decreasing the crystal size and modifying the grain boundaries with CH_3COO^- .^[28] Besides the component adjustment, Park et al. demonstrate that the $CsPbI_2Br$ films with optimized crystallization exhibit dramatic phase stability against moisture atmosphere.^[29] Overall, the $CsPbI_2Br$ films present considerable phase stability when sandwiched between electron transport layer (ETL) and hole transport layer (HTL), and thus the corresponding PSCs have shown long-term stability with proper encapsulation.^[30]

3.3. Light Stability

Photo-induced phase segregation is observed as a common phenomenon in MA-based hybrid perovskites, even in materials with single halide components like $MAPbI_3$ and $MAPbBr_3$.^[31] This segregation becomes more serious in the mixed-halide perovskites ($MAPb(Br_xI_{1-x})_3$), resulting in formation of I- and Br-rich domains.^[32] The photo-induced halide segregation seriously damages the device performance, leads to open-circuit voltage (V_{oc}) decrease and photo-induced traps. It is demonstrated that the photo-induced halide segregation is affected by lattice strain, traps, light intensity, pressure, or compositional uniformity, but the origin is still unclear.^[33] Since the halide segregation is as the result of ion migration, therefore, it can be suppressed by increasing the ion migration barrier.

The light stability of cesium-based lead mixed-halide inorganic perovskites was first investigated by McGehee et al.^[34] A series of $CsPb(Br_xI_{1-x})_3$ films with different compositions have been illuminated under a fluence of 100 mW cm^{-2} . The photoluminescence (PL) peak position has been recorded over time. The PL peak position keeps constant when $0 \leq x \leq 0.4$, which presents a broader range of stable compounds in comparison with the $MAPb(Br_xI_{1-x})_3$ perovskites (compositions are stable when $0 \leq x \leq 0.2$).^[35] When $0.4 < x < 1$, phase segregation happens and both I-rich and Br-rich domains appear under illumination, as evidenced by the PL peak position shifts. But luckily, the phase segregation can be suppressed in high quality $CsPbI_2Br$ films. Similar suppression of the halide segregation has also been observed by Zhou et al.^[30b] The PL spectra of $CsPbI_2Br$ perovskite film under ultra-intense laser irradiation ($10\,000\text{ mW cm}^{-2}$) was recorded over time. As presented in Figure 3a, no peak shift is observed after 4 min irradiation. In contrast, the PL peak of hybrid perovskite $MAPb(I_{0.5}Br_{0.5})_3$ shifts immediately once turn on the same laser within 1 ms, indicating there is a serious and rapid halide segregation (Figure 3b).

As suggested above, the cesium-based mixed-halide inorganic perovskites have better light stability than the hybrid perovskites. Zhao et al. have quantitatively compared the photo-induced ion migration between the hybrid $MAPbI_3$ perovskites and the all-inorganic $CsPbI_2Br$ films.^[30b,36] The high-field electrical poling ($\approx 2\text{ V }\mu\text{m}^{-1}$) experiments using an Au/perovskites/Au lateral device structure have been performed to macroscopically observe the in situ ionic motion under different illumination

conditions. As shown in Figure 3c, no obvious change of the $MAPbI_3$ film is observed in the dark. Whereas under illumination, ion migration induces the formation of a new phase (PbI_2 segregation forms a black line) within 10 s of poling. The stronger light intensity, the severer ionic motion. Note that this light-induced ionic motion is independent of the halide (I/Br) ratio and the gaseous environment (air or vacuum). In contrast, for the $CsPbI_2Br$ film, no phase segregation has been observed under a much stronger light for over 20 s (Figure 3d). The much better light stability of Cs-based perovskites indicates that either the ion migration barrier is higher or the ion migration is independent of light, when compared to that of MA-based perovskites.

In order to quantitatively analyze the ion migration, the light intensity-dependent energy barrier of ion migration (E_a) has been extracted from cryogenic galvanostatic and voltage-current measurements (Figure 3e,f). The E_a of $MAPbI_3$ strikingly decreases from 0.62 to 0.07 eV when the light intensity increases from 0.1 to 25 mW cm^{-2} . The low ion migration barrier under strong light causes severe ion migration in $MAPbI_3$ film, leading to a fast degradation of the PSC burn-in field. In contrast, the E_a of $CsPbI_2Br$ is light intensity-independent (from 0.45 to 0.43 eV). Cesium substitution eliminates the light-induced ionic motion, highlighting that organic cations play key roles in the complicated interplay between ionic transport and photon excitation. Gottesman et al. demonstrates the binding between the MA^+ ions and the inorganic frames weakens under illumination, and thus leads to a softer $MAPbI_3$ lattice, which might contribute to the light-enhanced ion migration.^[37] Polaron with a deformed lattice surrounding the photocarriers forms in both $MAPbBr_3$ and $FAPbBr_3$, but excluding $CsPbBr_3$.^[38] Both polaron formation and ionic motion are organic cation-dependent, suggesting another potential mechanism for light-enhanced ion migration.^[39] Overall, the $CsPbI_2Br$ exhibits high ion migration barrier and light intensity-independent ionic motion, which leads to an excellent light stability against the photoinduced phase segregation.

Taken together, the $CsPbI_2Br$ has superior stability against heat, moisture and illumination, leading to long-term stability for over 1500 h of the corresponded PSCs under continuous light illumination and steady-state operation tracking at the maximum power point (Figure 3g).^[30b] This highlights the superior electric field resistibility of inorganic $CsPbI_2Br$ perovskite, sustaining a bright future in PSCs development. In spite of delectable stability of $CsPbI_2Br$, the moisture stability is still hard to overcome. This opportunity invites further improvements on the perovskite material and device interface properties, and also new encapsulation materials and technologies.

4. Performance Improvement

The PCEs of $CsPbI_2Br$ PSCs rapidly improve to 14.8% within only 2 years. Depositing high-quality thin films through crystallization control is the primary step toward high-performance devices. Besides, both the defect passivation and the interface engineering significantly contribute to the high PCE values. How these three major aspects affect the PSC performance are reviewed in this part.

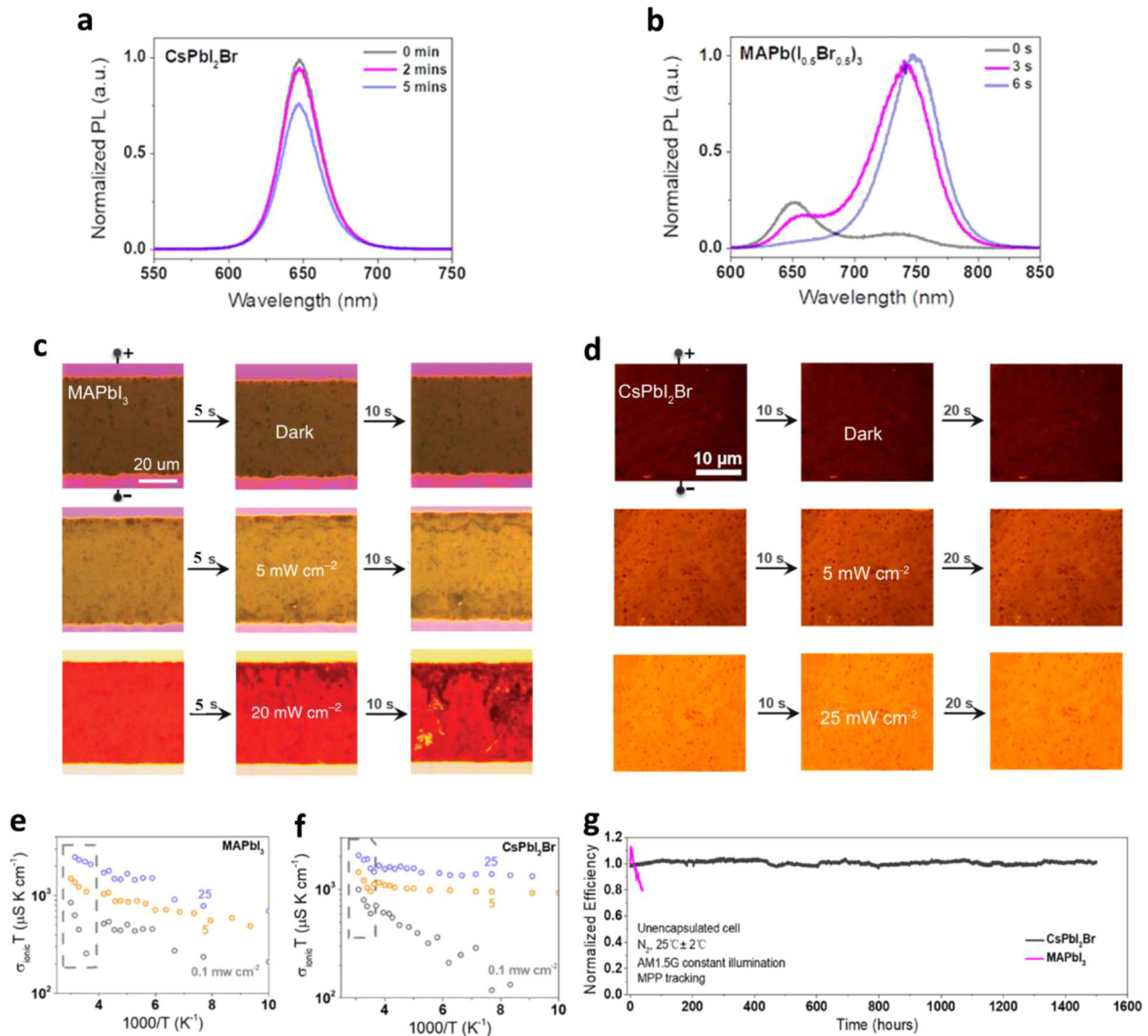


Figure 3. PL spectra for (a) CsPbI₂Br, and (b) MAPb(I_{0.5}Br_{0.5})₃ perovskite films over time under 10⁴ mW cm⁻² light intensity in ambient air. Optical dynamic images of (c) MAPbI₃ and (d) CsPbI₂Br perovskite films under electric poling and illumination of various intensities in ambient air at room temperature. Ionic conductivity of (e) CsPbI₂Br and (f) MAPbI₃ films. g) Continuous maximum point tracking for unsealed CsPbI₂Br and MAPbI₃ solar cells over 1500 h in a nitrogen glovebox at room temperature. Figure 3c is reproduced under the terms and conditions of the Creative Commons Attribution-NonCommercial-NoDerivs 4.0 International License.^[36] Copyright 2017, The Authors, published by Springer Nature. Figures 3a,b and 3d–g are all reproduced with permission.^[30b] Copyright 2017, American Chemical Society.

4.1. Crystallization Control

4.1.1. One-Step Solution-Processed Films

Deposition of high-quality CsPbI₂Br film is challenging, mainly suffering from the solubility limitations of CsBr. Therefore, crystallization control during film deposition is critical toward high-performance CsPbI₂Br PSCs. A two-step method has been firstly developed to overcome the solubility limitation problem in CsPbBr₃ solar cells.^[40] However, this method is helpless in obtaining uniform and smooth Cs-based mixed-halide perovskite films. Snaith et al. first obtained high-quality CsPbI₂Br thin

films via a one-step method.^[16] The thickness of this perovskite film is only 150 nm, due to the limited solubility of CsPbI₂Br in DMF (0.4 M). The corresponded PSCs present a dramatic PCE of 9.8% from a reverse current–voltage (*J*–*V*) scan, together with significant hysteresis and thus deliver stabilized power outputs (SPO) of only 5.6%. Almost at the same time, McGehee et al. fabricated the inverted CsPbI₂Br PSCs using DMSO as solvent.^[34] The improved device structure promotes the SPO to 6.5% with negligible hysteresis. Soon after, Park et al. discovered that optimizing the crystallization process through controlling the annealing temperature improves the film phase stability and PSC PCEs. The champion device shows a PCE of 10.7% and SPO

of 9.5%.^[29] But the limited CsPbI₂Br active layer thickness still hinders the device performance, particularly the J_{sc} , and higher device PCEs are expected to be achieved with thicker films maintaining the superior morphology.

In order to increase the solubility of Br ion, Dimethyl Sulphoxide (DMSO) with stronger polarity and coordination ability has been introduced into DMF as co-solvent. This technique promotes the solubility of CsPbI₂Br to 1.2 M, offers films with the thickest thickness over 500 nm.^[14b,24a] Mariotti et al. added 10% DMSO to DMF and fabricated active layers using a 50 °C precursor solution, resulting in a 350 nm-thick CsPbI₂Br film. But the as-prepared perovskite films are abundant with pin-holes and the corresponded devices give the peak efficiency of 9.08%.^[41] Zhao et al. fabricated a 300 nm CsPbI₂Br film with mixed DMSO/DMF, achieving a 10.3% champion PCE.^[30b] Ho-Baillie et al. employed a mixed solvent with the DMF:DMSO ratio of 2:1 and a gas assisted spin coating method, and obtained a 250 nm-thick CsPbI₂Br absorber with an efficiency of 7.7%.^[42] Although active layers with enough thickness for sufficient light harvesting have been obtained, the PSC PCEs are still lag behind due to the poor film morphology and crystallinity (leading to deficient charge carrier transport and collection).

Understanding the effects of solvents on CsPbI₂Br crystallization and growth is critical to optimize film morphology and increase the grain size. The DMF/DMSO mixture are often employed to prepare dense and smooth organic-inorganic hybrid perovskite films. There is a strong coordination between DMSO and Pb²⁺, which can suppress the crystallization of PbI₂ and perovskite.^[43] Particularly, an intermediate phase MAI-PbI₂-DMSO exists in the spin-coated film, and gradually releases DMSO in the following annealing step, which would promote the perovskite crystallization toward high-quality films. Besides, solvent composition also plays a vital role on the intermediate phase formation and the perovskite crystal growth.^[44] Recently, Chen et al. conducted a systematic study on how the solvent composition effects the morphology, crystallization, and photoelectric property of CsPbI₂Br films.^[24b] The precursors were dissolved in mixed solvents with six different DMSO contents (0vol% DMSO, 5vol% DMSO, 20vol% DMSO, 40vol% DMSO, 80vol% DMSO, 100vol% DMSO), and the perovskite films were deposited using an anti-solvent-extraction technology with the aid of diethyl ether. The reference CsPbI₂Br (0% DMSO sample) shows a faster crystallization than that of the hybrid MAPbI₃ at room temperature, which is attributed to the lower energy barrier for intercalating Cs⁺ into PbX₂ frameworks (the Cs⁺ radius is 0.18 nm, much smaller than 0.27 nm of MA⁺). Nevertheless, intermediate phase PbX₂-CsI-DMSO forms when the DMSO ratio exceeds 40%, as evidenced by the two emerging peaks at 6.7° and 10.1°, respectively (Figure 4a). After annealing, the 40% DMSO sample presents the best crystallinity with smooth surface morphology, which is benefiting from the intermediate phase PbX₂-CsI-DMSO (Figure 4b). However, when taking an overdoses of DMSO (the 80% and 100% DMSO samples), the grain size decreases and more pinhole forms. Furthermore, the 40% DMSO sample presents the lowest Urbach energy, the bluest PL peak location, the narrowest emission width, and the longest emission lifetime (Figure 4c–e), which implies the minimum number of defects and the most

perfect crystallization. Finally, a PCE of 9.14% and a high J_{sc} of 14.2 mA cm⁻² have been achieved based on this optimized 40% DMSO film (410 nm). Tian et al. further introduced a heat-assisted reaction of the hot air flow (HAF) procedure to control the CsPbI₂Br crystallization from the DMF/DMSO mixed-solvent. The high-quality CsPbI₂Br films were obtained in a wide solution-processing window, involving a wide range of solute concentrations and solvent components. The optimized device exhibits a PCE of 12.52% and delivers the highest V_{oc} up to 1.315V.^[45]

On the basis that DMSO-assistant CsPbI₂Br growth can lead to high-quality thick films, more recently, You et al. developed a new solvent-controlled growth (SCG) method to slow down the evaporation rate of the residual DMSO, which decreases the nucleation and growth rate.^[46] The SCG process represents for placing the precursor films in the nitrogen glove box for several 10 min at room temperature before annealing. Mixed DMSO/DMF were used to dissolve the perovskite precursors. Smooth and dense CsPbI₂Br films with large grain size up to several micron-meters were obtained using the SCG process (Figure 4f, g), and thus an impressive PCE of 14.21% was obtained from the corresponded PSCs (Figure 4h).

Besides solvent engineering, ion doping can also promote the crystal growth. Liu et al. utilized Mn²⁺ doping to modulate crystal growth, leading to the CsPbI₂Br grain size increase with an aspect ratio as high as 8 (Figure 5a,b). Doping Mn²⁺ into the CsPbI₂Br lattice interstice reduces the crystal nucleation and growth rate, thus resulting in better crystallinity with larger grains. In addition, excess Mn²⁺ ions aggregate at the film surface and the grain boundaries passivating defects, leads to reduced recombination loss and enhanced charge extraction efficiency. A dramatic efficiency of 13.47% is eventually obtained (Figure 5c), with an 13% improvement compared to that of the control device (PCE of 11.88%).^[47] Liu's group further found that the precursor solution temperature also influences the crystallization process of CsPbI₂Br.^[17a] The nucleation step seriously depends on the precursor solubility, and the solvent evaporation rate largely affects the crystal growth rate. Therefore, crystallization control is realized through optimizing the precursor solution concentration and temperature. The most suitable temperature of the precursor solution for CsPbI₂Br film fabrication is 100 °C from a systematic research. The champion device produces a PCE of 14.81%, which is the highest value among CsPbI₂Br PSCs to date. More recently, the Lewis base adducts PbX₂(DMSO) (X = Br, I) have been found to slow the crystallization rate of CsPbI₂Br and thus improve the film quality.^[48] High quality CsPbI₂Br films showing flat surfaces, large-scale crystalline grains, long carrier lifetimes (Figure 5d), and few defects were obtained, resulting in a considerable PCE of 14.78% (Figure 5e). The trap densities, determined using the space-charge-limited current (SCLC) method, decrease from 1.94 × 10¹⁶ cm⁻³ (control device) to 3.64 × 10¹⁵ cm⁻³ (Figure 5f). This value is comparable to that of the MA-based hybrid polycrystalline perovskite film, but still greater than that of the perovskite single crystals.^[49] Further studies on crystallization control to obtain high-quality film with larger crystalline grain size and less traps are needed.

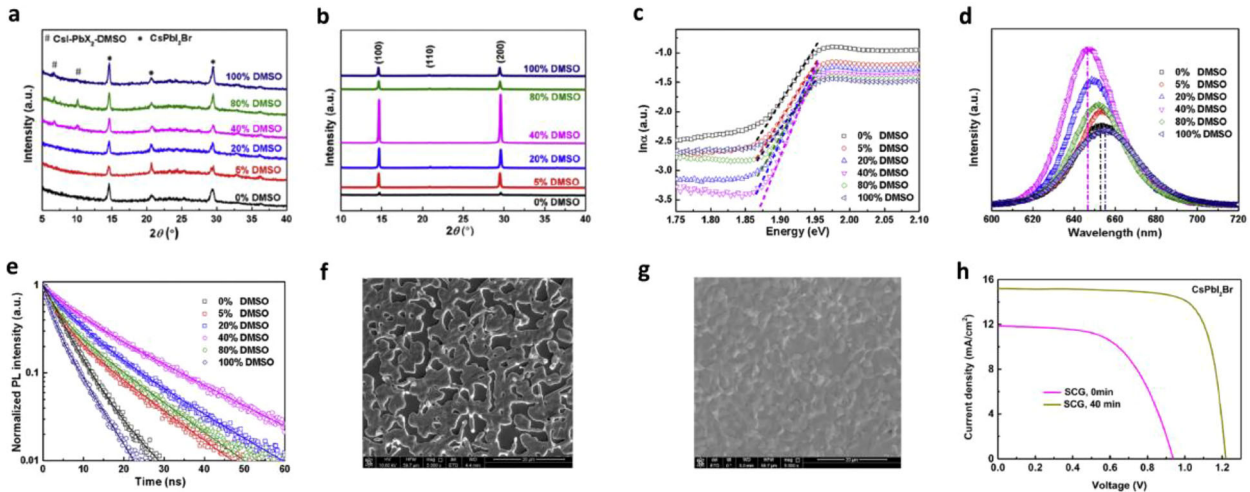


Figure 4. a) XRD patterns of the as-prepared films before annealing. b) XRD patterns of annealed perovskite films. c) UV-vis absorption spectra, (d) steady state PL spectra and (e) time-resolved PL spectra of annealed perovskite thin films from precursor solutions with different DMSO volume ratios. Reproduced with permission.^[24b] Copyright 2018, Elsevier. Scanning electron microscopy (SEM) images of CsPbI₂Br film (f) without solvent controlled growth (SCG) and (g) with SCG procedure. (h) J–V curves of the CsPbI₂Br PSCs without and with SCG procedure. Reproduced with permission.^[46] Copyright 2018, Nature Publishing Group.

4.1.2. Films Deposited From Colloidal Nanocrystal Solution

Perovskite nanocrystals (NCs) have attracted increasing attentions for optoelectronic applications, due to their near-unity photoluminescence quantum yield, tunable bandgap, and low trap state density.^[50] Analogous to the well-established deposition method for CdTe and PbS NC solar cells, the perovskite films can also be assembled via a layer-by-layer (LBL) spin-coating procedure from colloidal NCs.^[51] The surfactants capping the NC surfaces make the NCs dispersing homogeneously in the nonpolar solvent, thus the NC solution exhibits excellent film-forming abilities independent on substrates. Besides, the film thickness can be easily tuned by the solution concentration and the deposition number of times. However, the long-chain insulated surfactants significantly impede electron coupling between the NCs. Therefore, the ligand exchange is essential to fabricate high-efficiency solar cells. Yang et al. developed a valid method to deposit high-quality CsPbI₂Br films from colloidal NCs (Figure 6a).^[52] The electrically insulating ligands are removed efficiently by soaking the NC film in anhydrous isopropanol (IPA) (Figure 6b). Meanwhile, the NCs begin to reassemble and grow once getting in touch to IPA solution, and grow further to form continuous film after annealing. They combined this CsPbI₂Br NC film with poly(3-hexylthiophene) (P3HT) to construct planar heterojunction. The P3HT passivates surface defect states to reduce interfacial electron-hole recombination (Figure 6c). The density functional theory (DFT) calculations indicate that the sulfur (S) atoms of P3HT bond with Cs atoms (Cs–S: 4.03 Å) and passivate the positively charged under-coordinated Cs⁺ ions on the CsPbI₂Br (110) surface (Figure 6d,e). Besides, S atoms also bond with Pb atoms (S–Pb: 3.36 Å) to passivate the deep-level defects (antisite defects), which are the most detrimental defects in perovskite solar cells (Figure 6e,f). In addition, the energy disorder of P3HT hole transport layer reduces after a simple annealing process

(Figure 6g). Finally, a PCE of 12.02% (Figure 6h), and a V_{oc} of up to 1.32 V with energy losses (E_{loss}) down to 0.5 eV from a reverse scan are achieved through modifying the perovskite films with annealed polythiophene. Noting that the whole device fabrication process is conducted under ambient air conditions.

Shortly afterwards, Konstantatos et al. fabricated CsPbI₂Br NC solar cells without annealing process.^[53] They deposit the CsPbI₂Br NC films via two different methods: the LBL process and the single-step (SP) deposition. They find the PSCs from the SP approach show higher V_{oc} of 1.31 V, while the LBL devices present more suppressed hysteresis (Figure 6i), which is consistent with previously reported NC PSC results.^[11]

Another advantage is that the CsPbI₂Br NC films present excellent photostability with suppressed light-induced phase segregation.^[54] Colloidal NCs provide an efficient procedure to deposit high-quality inorganic perovskite films under ambient air conditions. However, the ligand exchange mechanism is essentially different from the well-established rules of conventional covalent semiconductor NCs, because of the ionic nature of perovskite NCs. Therefore, optimizing ligand exchange process is critical to further enhance the electronic coupling and maximize the long-range charge transport in perovskite NC films.

4.1.3. Vacuum-Deposited Films

Currently, most researches mainly focus on solution-processed perovskite films due to the rapid energy payback time. The vacuum deposition also provides a promising procedure to fabricate high-quality perovskite films with good uniformity and high reproducibility. Lin et al. first developed a controllable method to deposit homogeneous CsPbI₂Br films.^[30a] The as-deposited CsPbI₂Br thin film presents substantially small crystalline domain size of 100 nm. After annealing, the grain

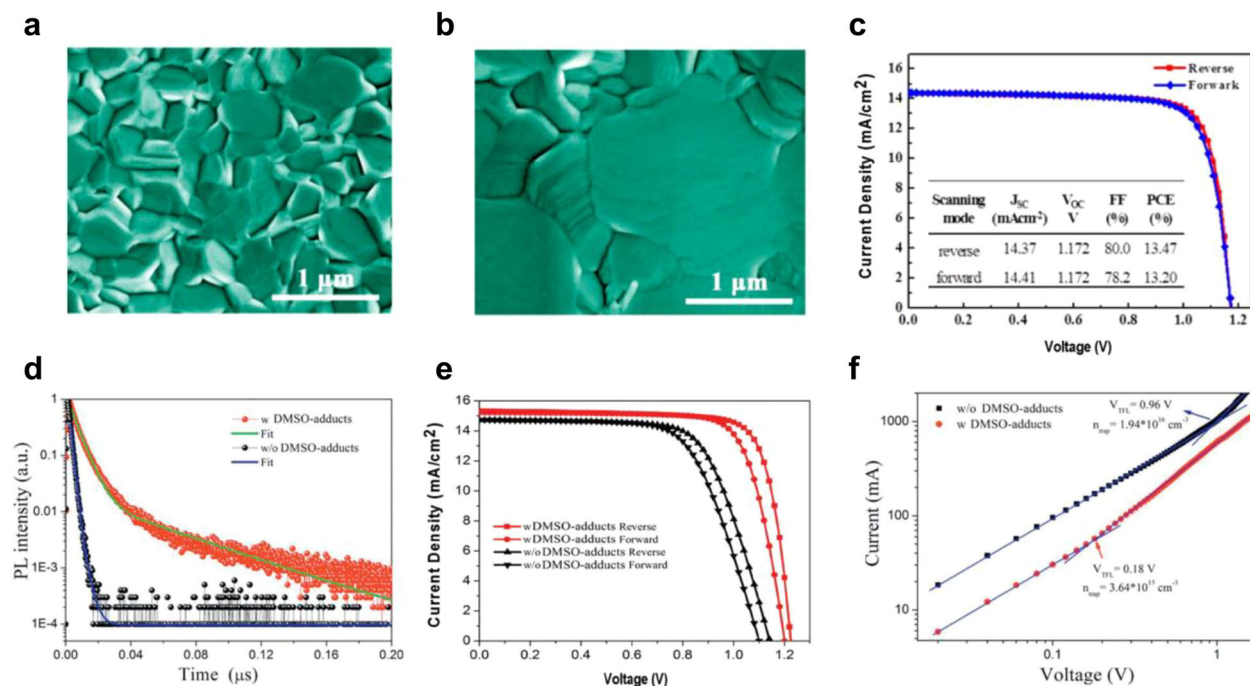


Figure 5. SEM images of the CsPbI₂Br films (a) without and (b) with 2% MnCl₂. c) *J*–*V* curves of the champion device based on 2% MnCl₂ doped CsPbI₂Br. Reproduced with permission.^[47] Copyright 2018, American Chemical Society. d) TRPL of CsPbI₂Br films prepared without and with DMSO adducts. e) *J*–*V* curves of the CsPbI₂Br PSCs fabricated with and without DMSO-adducts. f) *J*–*V* curves of devices (FTO/TiO₂/CsPbI₂Br/PCBM/Ag) fabricated with and without DMSO adducts. Reproduced with permission.^[48] Copyright 2018, Wiley–VCH.

size becomes as large as 3 μm. After assembling the active layer with vacuum-sublimed electron and hole transport layers, all-vacuum-deposited CsPbI₂Br PSCs exhibit negligible hysteresis with considerable PCE of 11.8% and SPO up to 11.5%. These values reached the record PCE of Cs-based inorganic PSCs at that time. Besides, the devices show impressive PCE of 26.6% under 1000 lux fluorescent light. In addition, they demonstrate that the films with stoichiometrically balanced precursor ratios present significantly better photovoltaic performances than those with nonstoichiometric molar ratios, which is consistent with the results of Ho-Baillie et al.^[55]

4.1.4. Low-Temperature Processed Films for Flexible Devices

In general, the CsPbI₂Br films require a high-temperature annealing process (>260 °C) to obtain photovoltaic-active cubic phase and large crystalline domains with good charge transport. However, the annealing process is energy-consuming and undesirable for flexible and multijunction tandem solar cells. It is challenging to fabricate high-quality CsPbI₂Br films via a low-temperature (<150 °C) solution-processed procedure. Ho-Baillie et al. found the low-temperature-processed (100 °C) high-performance CsPbI₂Br PSCs can be fabricated through the strontium (Sr) doping.^[42] The Sr ions mainly cover the surface of perovskite crystals and passivate the surface defects, leading to enhanced charge lifetime. The champion CsPb_{0.98}Sr_{0.02}I₂Br PSC delivers a PCE of 11.3% and a SPO of 10.8%. Recently, Zhao et al. reported a facile method to deposit cubic CsPbI₂Br film with low

annealing temperature at 130 °C.^[56] In this method, the I-excess precursor of HPbI_{3+x} ($x = 0.1–0.2$) was used to replace the PbI₂ and forms a new precursor of 2CsI+HPbI_{3+x}+PbBr₂. A smooth and compact precursor film has been prepared with the new precursors by a one-step spin coating process. After annealed at a mild temperature of 130 °C, the grain size increases from less than 100 nm to 300–400 nm. The champion efficiency of 10.5% has been obtained from a reverse scan. Besides, the facile-deposited CsPbI₂Br films exhibit excellent long-term phase stability and thermal stability. Recently, Rao et al. found the as-deposited non-perovskite CsPbI₂Br film rapidly transforms into black cubic phase through a room-temperature solvent (DMSO) annealing (RTSA) treatment (Figure 7a).^[57] The solar cells from the room-temperature-deposited CsPbI₂Br film exhibit a maximum PCE of 6.4%, while the efficiency boosts up to 10.4% after the RTSA-treated CsPbI₂Br film sintered at low-temperature of 120 °C. Moreover, they fabricated the first flexible inorganic PSCs, showing a considerable PCE of 7.3% (Figure 7b). The flexible CsPbI₂Br PSCs have good mechanical flexibility, and maintain the initial efficiency even after 100 bending cycles at a fixed bending radius of 10 mm (Figure 7c). More recently, Liu et al. replaced PbX₂ (X = Br, I) precursors with PbX₂(DMSO) (X = Br, I) adducts, which allowed to form CsPbI₂Br perovskites via a low activation energy route. The flexible CsPbI₂Br devices based on the low-temperature-processed (120 °C) perovskites present good stability and superior efficiency up to 11.73%.^[8a] These works indicate the high-quality CsPbI₂Br films can be achieved at low annealing temperature through controlling the perovskite crystallization dynamics, pointing out the potential of

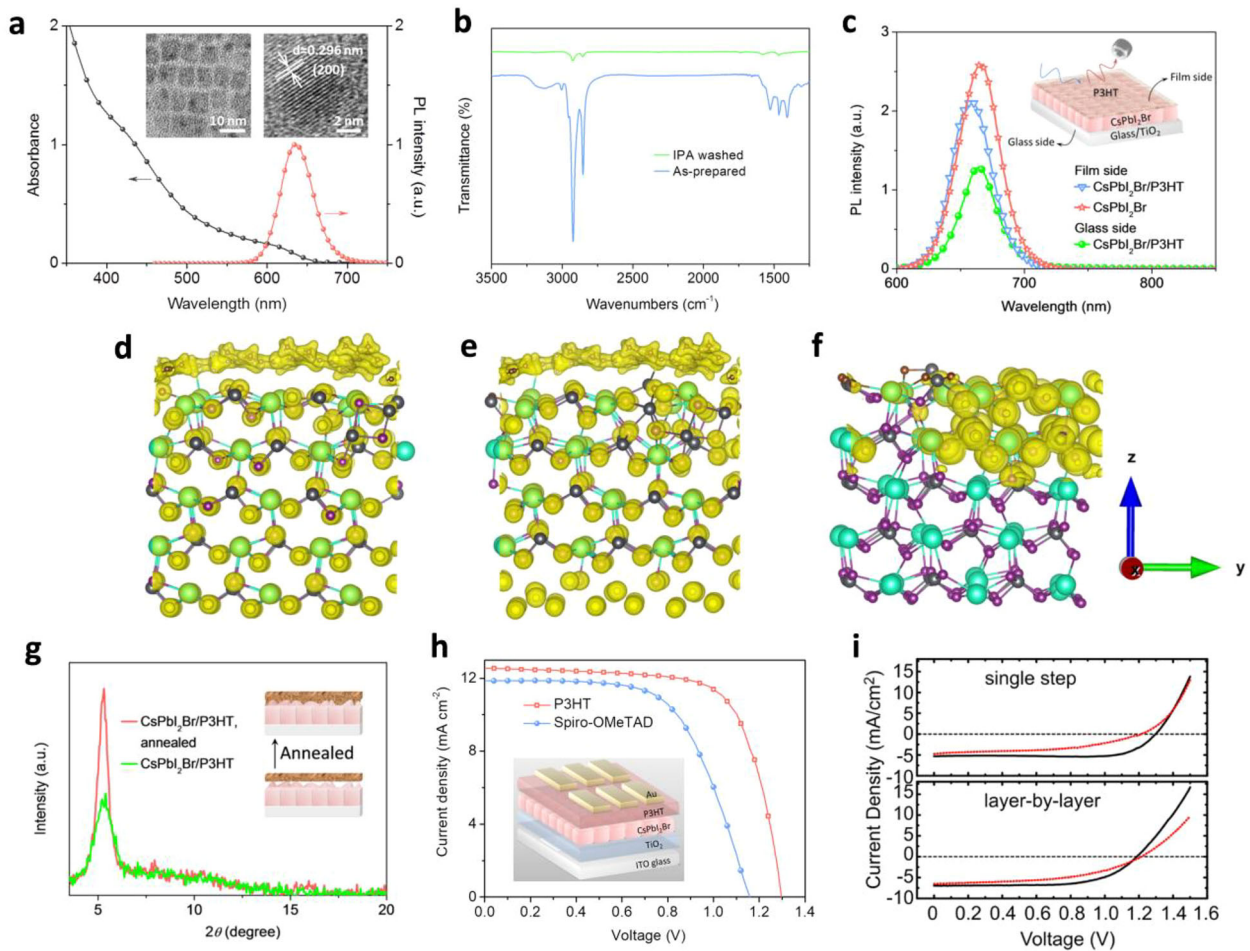


Figure 6. a) UV-visible absorption and PL spectra of CsPbI₂Br NCs. Insets are TEM (left) and HRTEM (right) images of CsPbI₂Br NCs. b) FTIR spectra of CsPbI₂Br NC films before and after isopropyl alcohol (IPA) treatment. c) The steady-state PL spectra for CsPbI₂Br film and P3HT/CsPbI₂Br bilayers excited using a 405 nm laser from different side of the sample. Inset is the schematic of PL experiment setup. Density distribution plots of (d) P3HT on CsPbI₂Br 110-surface, (e) P3HT on CsPbI₂Br 110-surface with antisite defects, and (f) pure CsPbI₂Br 110-surface with antisite defects. (g) XRD patterns of P3HT/CsPbI₂Br bilayers before and after 200 °C annealing. Inset presents schematic diagram of the interface evolution during the annealing process. h) *J*-*V* curves of the CsPbI₂Br solar cells using P3HT and spiro-OMeTAD HTLs. Inset is the device structure. Reproduced with permission.^[52] Copyright 2018, Wiley-VCH. i) Reverse and forward *J*-*V* curves of the solar cells from single step and layer-by-layer strategies. Reproduced with permission.^[53] Copyright 2018, American Chemical Society.

all-inorganic CsPbX₃ perovskites for flexible electronic applications. Preparing flexible photoelectronic devices from colloidal NCs is also promising, since the annealing process is not necessary for assembling the cubic CsPbI₂Br NCs to perovskite films.

4.2. Defect Passivation

Passivating defects is critical for achieving high carrier mobilities, long carrier lifetime and long carrier diffusion length. The defects at the crystal surface and grain boundaries will generate trap states and are detrimental to the device stability.^[58] These trap states not only harm the device photocurrent output through decreasing the charge carrier diffusion length, but also decrease the device *V*_{oc} through increasing the energy disorder and reducing the carrier

concentration, which pull down the quasi-Fermi level splitting. Thus, electronically passivating the defects is highly desirable to boost the PSC performance.

As above mentioned, both the polymer (P3HT) and the ions (Sr²⁺ and Mn²⁺) can passivate the trap states at the surface and grain boundaries, resulting in improved device performance. Besides, Stranks et al. demonstrated that decorating the surfaces and grain boundaries of perovskites with potassium passivation reduces the non-radiative losses efficiently.^[59] Park et al. first adopted the potassium passivation to promote the performance of inorganic CsPbI₂Br PSCs, and they achieved a PCE of 10.0% based on the optimal composition of Cs_{0.925}K_{0.075}PbI₂Br.^[60] Besides, the potassium incorporation efficiently enhances the material stability, and thus the device stability. Furthermore, Han et al. added a small amount of Pb(Ac)₂ into the CsPbI₂Br precursors.^[28] The Pb(Ac)₂ validly embellishes at the CsPbI₂Br grain boundaries, and in situ decomposes into semiconducting

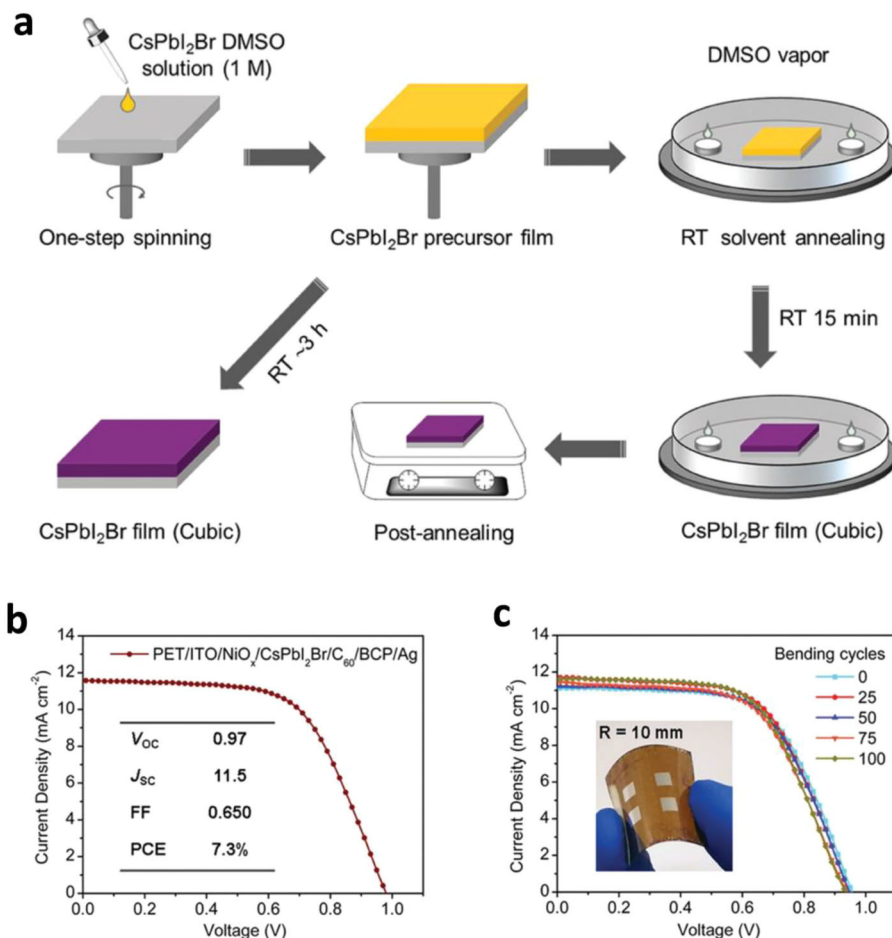


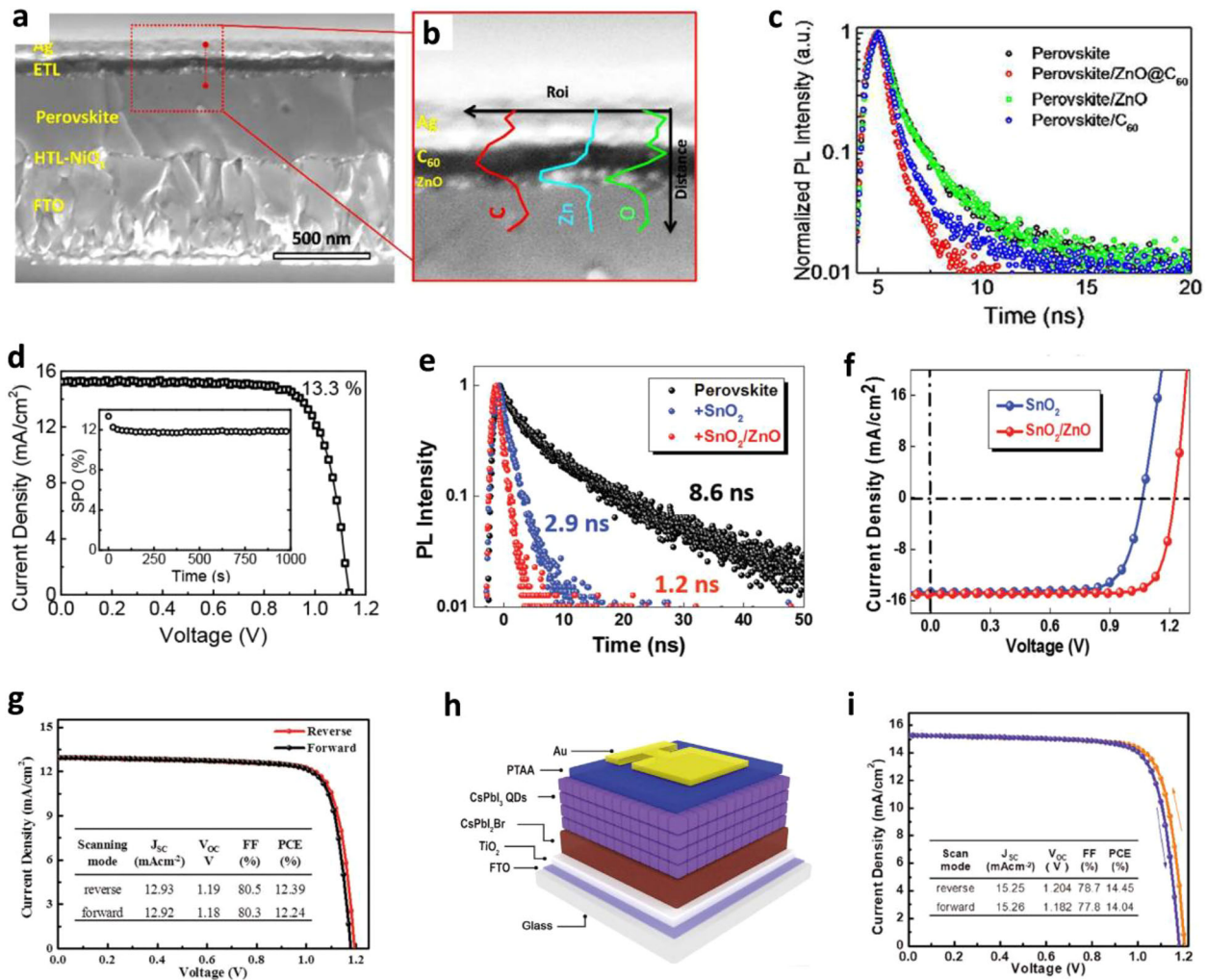
Figure 7. a) Preparation of CsPbI₂Br films from room temperature DMSO vapor annealing and direct thermal annealing procedures, respectively. b) J–V curves of the champion flexible CsPbI₂Br device. c) Device performance evolution of the flexible device over bending cycles. A photograph of the flexible solar cell is given as inset. Reproduced with permission.^[57] Copyright 2018, Wiley–VCH.

PbO after annealing, which effectively passivates the surface defects, reduces recombination loss, and improves charge transport for the CsPbI₂Br films. Therefore, the PbO-passivated CsPbI₂Br PSCs exhibit a 12% efficiency with good stability, much better than the control devices with a PCE of 8.5% and inferior stability. More recently, Tian et al. found Pb(NO₃)₂ could passivate the CsPbI₂Br surface defects, which results in reduced trap states density and enhanced hole transfer rate, thus getting an improved PCE of 12.34% and a V_{oc} of up to 1.29 V.^[61] The defect engineering in inorganic perovskites are still at their initial stage, and new passivation strategies should be further developed. More efforts should be paid on identifying the defect types and repairing them, in order to achieve high-quality CsPbI₂Br films with reduced recombination loss for high-performance solar cells.

4.3. Interface Engineering

The charge carrier loss happens when there is a mismatch in energy levels between the perovskite film and ETL or HTL.^[62] Thus, synergic optimization of the device interface is of great

urgency to reduce recombination loss and improve charge collection toward highly efficient CsPbI₂Br PSCs. The optimized device structure also contributes to cell stability. Mai et al. utilized ZnO/C₆₀ bilayer as the ETL, developed a novel inverted device construction of FTO/NiO_x/CsPbI₂Br/ZnO/C₆₀/Ag, as shown in **Figure 8a,b**.^[24a] The superior electron-extracting capability of ZnO/C₆₀ bilayer is higher than either ZnO or C₆₀ alone (Figure 8c). The optimized CsPbI₂Br PSCs delivers a PCE of up to 13.3% with a remarkable SPO of 12% (Figure 8d). Besides, the PSCs based on this new device structure exhibits excellent thermal stability with only 20% PCE loss after being heated at 85 °C for 360 h without encapsulation. More recently, Yip et al. introduced SnO₂/ZnO bilayer ETL into the conventional normal architecture (ITO/SnO₂/ZnO/CsPbI₂Br/Spiro-OMeTAD/MoO₃/Ag).^[17b] The higher-lying conduction band minimum (CBM) of ZnO (–4.21 eV) facilitates desirable cascade energy level alignment with the CsPbI₂Br perovskite, which is propitious to reduce the energy loss of charge transfer. Compared to the individual ZnO or SnO₂, the SnO₂/ZnO bilayer exhibits superior electron extraction capability (Figure 8e), which leads to reduced interfacial trap-assisted recombination. Combining SnO₂/



ZnO bilayer with the high-quality CsPbI₂Br film, the optimized PSC presents a PCE of 14.6% with a high *V*_{oc} up to 1.23 V (Figure 8f). More importantly, the SnO₂/ZnO-assistant CsPbI₂Br PSCs show a decent thermal stability with 80% PCE maintained after being heated at 85 °C for 300 h.

Apart from modifying the anode interface, Liu et al. developed a series of nice methods on modifying the cathode interface with nanomaterials, for example, the nanosheets and the quantum dots (QDs). A dimensionally graded heterojunction was constructed between the perovskite and HTL through distributing the CsPbI₂Br materials within bulk–nanosheet–QD or 3D–2D–0D dimension-profiled interface structure, which gives rise to graded energy alignment at the interfaces.^[63] The optimized energy alignment between the CsPbI₂Br and the HTL layer is benefitted for suppressed recombination loss during the hole-transfer process. Therefore,

this profiled structure induces continuously upshifted energy levels with enhanced hole extraction, leading to a PCE of 12.39% with impressive fill factor (*FF*) as high as 80.5% (Figure 8g). However, the efficiency of this device is mainly limited by the relatively low *J*_{sc} of only 12.39 mA cm⁻². To overcome this deficiency, CsPbI_{2+x}Br_{1-x} PSCs with graded bandgap has been fabricated using CsPbI₂Br and CsPbI₃ QDs as component cells, as shown in Figure 8h.^[64] The introduce of CsPbI₃ QD layer aims to achieve enhanced light harvesting as well as appropriate energy alignment. Through Mn²⁺ substitution, KSCN passivation, and [(NH₂)₂CH]⁺ treatment, stable and high-mobility CsPbI₃ QD films are obtained. The thickness of CsPbI₃ QD layer is systematically optimized in the graded bandgap structure. Finally, the device based on this novel architecture delivers an impressive PCE of 14.45% with *J*_{sc} up to 15.25 mA cm⁻² (Figure 8i).

Table 1. A summary of the experimental conditions, device structure, and detail performance parameters of reported CsPbI₂Br solar cells up to now.

Atmosphere	Method [Solvent, Anneal °C]	Device structure	Thickness [nm]	J_{sc} [mA cm ⁻²]	FF	V_{oc} [V]	E_{loss} [eV]	PCE [%]	SPO [%]	Ref.
Air-free	Solution (DMSO, 135 °C)	ITO/PEDOT:PSS/P/PCBM/BCP/AI	150	10.9	–	1.06	0.84	6.8	6.5	[34]
Air-free	Solution (DMF, 350 °C)	FTO/c-TiO ₂ /P/Spiro/Au	150	11.89	0.75	1.11	0.81	9.84	5.6	[16]
Dry-air	Solution (DMF, 280 °C)	FTO/c-TiO ₂ /Cs _{0.925} K _{0.075} PbBr ₂ / Spiro /Au	100	11.6	0.73	1.18	0.74	10.0	9.2	[60]
Air-free	Solution (DMF, 345 °C)	FTO/c-TiO ₂ /P/Spiro/Au	150	13.99	0.67	1.10	0.8	10.34	–	[8b]
Dry-air	Solution (DMF, 280 °C)	FTO/c-TiO ₂ /P/Spiro/Au	85	12.0	0.73	1.23	0.69	10.7	9.5	[29]
Air-free	Vacuum-Deposited (260 °C)	ITO/Ca/C ₆₀ /P/TAPC/TAPC:MoO ₃ /Ag	400	15.2	0.68	1.13	0.69	11.8	11.5	[30a]
Air-free	Solution (DMF/DMSO, 280 °C)	FTO/c-TiO ₂ /P/Spiro/Au	300	–	–	1.19	0.73	10.3	9.3	[30b]
Air-free	Solution (DMF/DMSO, 100 °C)	FTO/c-TiO ₂ /m-TiO ₂ / CsPb _{0.98} Sr _{0.02} I ₂ Br/ P3HT/Au	250	14.9	0.71	1.07	0.81	11.3	10.8	[42]
Air-free	Vacuum-Deposited (300 °C)	FTO/c-TiO ₂ /P/P3HT/Au	230	11.5	0.67	1.01	0.89	7.7	6.7	[55]
Open-air	Solution (DMF, 130 °C)	FTO/c-TiO ₂ /P/Spiro/Au	150	13.61	0.69	1.13	0.77	10.50	–	[56]
Air-free	Solution (DMF/DMSO, 350 °C)	ITO/c-TiO ₂ /P/Spiro/Au	350	12.7	0.68	1.05	0.87	9.08	–	[41]
Open-air	QDs solution (Toluene, 265 °C)	ITO/c-TiO ₂ /P/P3HT/Au	200	13.13	0.70	1.30	0.52	12.02	9.5	[52]
Air-free	Solution (DMSO, 260 °C)	FTO/c-TiO ₂ /P(2%MnCl ₂)/CsPbI ₂ Br QDs/ PTAA/Au	200	14.37	0.80	1.17	0.74	13.47	13.37	[47]
Air-free	Solution (DMSO, 260 °C)	FTO/c-TiO ₂ /P/CsPbI ₂ Br NS/CsPbI ₂ Br QDs/ PTAA/Au	200	12.93	0.81	1.19	0.72	12.39	12.11	[63]
–	Solution (DMSO, 160 °C)	FTO/NiO _x /P/ZnO@C ₆₀ /Ag	500	15.2	0.77	1.14	0.78	13.3	12	[24a]
Air-free	Solution (DMF/DMSO, 260 °C)	FTO/NiMgLiO/P/PCBM/BCP/Ag	410	14.18	0.66	0.98	0.92	9.14	8.84	[24b]
Air-free	QDs solution (Octane)	FTO/c-TiO ₂ /CsPbI ₂ Br QDs/ Spiro/Au	140	5.32	0.77	1.31	0.57	5.34	–	[53]
–	Solution (DMSO, 100 °C)	ITO/SnO ₂ /P/Spiro/Au	500	14.27	0.70	1.1	0.8	10.99	–	[14b]
Air-free	Solution (DMF, 300 °C)	FTO/c-TiO ₂ /P/CsPbI ₃ QDs/PTAA/Au	–	15.25	0.79	1.20	0.71	14.45	14.41	[64]
Air-free	Solution (DMF/DMSO, 350 °C)	ITO/SnO ₂ /P/Spiro/Au	350	15.22	0.77	1.22	0.7	14.21	–	[46]
Air-free	Solution (DMSO, 120 °C)	ITO/NiO _x /P/C ₆₀ /BCP/Ag	300	12.6	0.78	1.05	0.85	10.4	8.0	[57]
Air-free	Solution (DMF/DMSO, 150 °C)	FTO/c-TiO ₂ /m-TiO ₂ / CsPbBr _{1.78} F _{0.22} /spiro/ Ag	–	14.94	0.68	1.01	0.85	10.26	–	[27]
Air-free	Solution (DMF/DMSO, 240 °C)	ITO/SnO ₂ /ZnO/P/ Spiro /MoO ₃ /Ag	400	15.0	0.79	1.23	0.69	14.6	–	[17b]
Air-free	Solution (DMF/DMSO, 350 °C)	FTO/c-TiO ₂ /m-TiO ₂ / P(5% Pb(Ac) ₂)/Spiro	–	13.98	0.74	1.17	0.73	12.0	–	[28]
Open-air	Solution (DMF, 340 °C)	FTO/c-TiO ₂ /P/Carbon	360	13.54	0.64	1.15	0.76	10.0	–	[8e]
Dry-air	Solution (DMF/DMSO, 280 °C)	FTO/c-TiO ₂ /m-TiO ₂ /P/ spiro/Ag	250	13.56	0.74	1.24	0.67	12.52	11.13	[45]
Open-air	Solution (DMF/DMSO, 200 °C)	FTO/TiO ₂ /P/Spiro/Au	300	15.33	0.79	1.22	0.68	14.78	14.67	[48]
Open-air	Solution (DMF/DMSO, 300 °C)	FTO/c-TiO ₂ /P/QDs/PTAA/Au	195	15.10	0.80	1.22	0.68	14.81	14.55	[17a]
Open-air	Solution (DMF/DMSO, 300 °C)	FTO/SnO ₂ /P/Spiro/Ag	200	12.41	0.77	1.29	0.62	12.34	11.50	[61]
–	Solution (DMF/DMSO, 120 °C)	PET/ITO/Nb ₂ O ₅ /P/Spiro/Au	300	14.61	0.67	1.19	0.71	11.73	11.63	[8i]
Open-air	Solution (DMF/DMSO, 300 °C)	FTO/SnO ₂ /CsPb _{0.8} Ge _{0.2} I ₂ Br/P3HT/Spiro/Au	360	12.15	0.70	1.27	0.62	10.8	–	[24c]

Every optimal parameter is highlighted with red color.

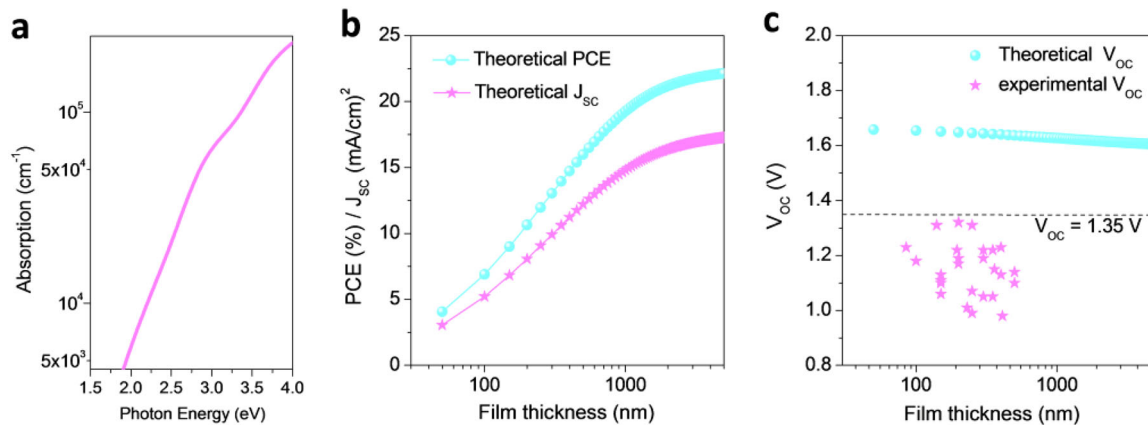


Figure 9. a) Calculated absorption spectrum of CsPbI₂Br. The optical absorption spectrum is calculated by considering the spin-orbit coupling (SOC) effect, with the Heyd-Scuseria-Ernzerhof (HSE) hybrid functional remedying the underestimation of band gaps in common DFT-PBE (Perdew, Burke, and Ernzerhof) calculations.^[65a] b) Simulated theoretical maximum PCE and J_{sc} of CsPbI₂Br PSCs as functions of film thickness based on “spectroscopic limited maximum efficiency” SLME method. c) V_{oc} of simulated theoretical maximum (azury sphere) and reported values (pink star) as functions of film thickness.

5. Challenges Toward High-Efficiency CsPbI₂Br PSCs

The detailed photovoltaic parameters of the reported CsPbI₂Br PSCs with device architectures and fabrication conditions are summarized in **Table 1**. In spite of the rapid progress, the efficiency of CsPbI₂Br PSCs is still far from the theoretical limit. We used the density functional theory (DFT) to calculate the theoretical intrinsic absorption coefficient of CsPbI₂Br, as presented in **Figure 9a**. We simulated the maximum PSC PCE under the standard AM1.5G solar spectrum at room temperature, through calculating spectroscopic limited maximum efficiency (SLME) employing the improved Shockley-Queisser model.^[65] The calculated FF almost maintains a high value around 0.918, which is much higher than the reported experimental values in high-performance PSCs. Thus a small correction on the calculation results is made by fixing the value of FF at 0.80, which has already been realized in inorganic CsPbI₂Br PSCs.^[17a,47,63] As shown in **Figure 9b**, the theoretical PCE of CsPbI₂Br PSCs is predicted up to 22.1% with an ultimate J_{sc} of 17.3 mA cm⁻², when the film thickness reaches 5 μm. The calculated V_{oc} slightly decreases from 1.65 to 1.60 V when increases the film thickness (**Figure 9c**). However, it is very challenging to thicken the CsPbI₂Br film in conventional methods. Fortunately, the CsPbI₂Br perovskite single crystal may be promising for 5 μm thick devices, using the methods developed by Chen et al.^[1] Typically, the perovskite single crystal with tuned thickness can be prepared using a hydrophobic interface confined lateral crystal growth method directly onto hole transport layers. However, the abundant defects on the single crystal surfaces are preventing the device efficiency enhancement. So much more works need to be done to reduce surface defects to improve the carrier collection and reduce the energy loss. When the CsPbI₂Br PSC delivers a J_{sc} of 16.3 mA cm⁻² and a V_{oc} of 1.5 V with FF of 0.8, the PCE is up to 19.6%, which is much higher than the state-of-the-art efficiency to date. These results are greatly

encouraging, but there remains a large scope to improve, especially for the V_{oc}. The V_{oc} for all of the reported CsPbI₂Br PSCs are lower than 1.35 V (**Figure 9c**), with the E_{loss} (the E_{loss} is calculated by the equation: E_{loss} = E_g - eV_{oc}) always higher than 0.65 eV. The E_{loss} has been reduced to 0.39 eV in hybrid PSCs.^[66] Therefore, it is highly promising to further improve the PCE of CsPbI₂Br PSCs through reducing the E_{loss} and enlarging the V_{oc}.

The challenges to the further improvements mainly present in continued reducing the electronic trap state densities. Improving charge carrier diffusion lengths of the CsPbI₂Br films to over 1 μm will significantly enhance the PSC performance, but demanding further trap state density reductions. The possible path to overcome this lies in surface and interface management, suggesting opportunities in both material chemistry and device physics. For material synthesis, a dense CsPbI₂Br film containing vertical growth perovskite crystals with the size of 1 μm is promising. In experiments, it is easy to obtain films containing parallel growth perovskite crystals with the size of 1 μm, but difficult for vertical growth CsPbI₂Br crystals of equal size. The precursors, temperatures, additives, defect passivation strategy, and so on are variables worthy of exploration. For device structure design, the accurate matching between active layer and HTL/ETL will facilitate the charge transport and reduce the energy loss. The CsPbI₂Br film has a valence band maximum (VBM) and a conduct band minimum (CBM) around -6.08 and -4.16 eV, respectively.^[24a] Employing ZnO (CBM: -4.21 eV) as the cathode interfacial layer matches well with CsPbI₂Br and can collect electrons efficiently. The main energy loss happens at the perovskite/HTL interface. Organic materials with such a deep highest occupied molecular orbital (HOMO) that match with the CsPbI₂Br are easily oxidized by oxygen, leading to instable PSCs. Therefore, searching and synthesizing new inorganic HTL materials with appropriate energy levels are critical and important for high-efficiency and high-voltage CsPbI₂Br PSCs.^[67]

6. Conclusion and Outlook

Simple solution-processed CsPbI₂Br solar cells offer cost advantages over conventional photovoltaics, and initial studies demonstrate acceptable device operational stability when insulating the moisture. Since commercially compelling needs PCEs over 15%, thus the most urgent task for CsPbI₂Br PSCs is to keep on pressing forward to better and better device performances. Efforts should be paid on both material chemistry and device physics toward this goal.

The device stability – mainly the moisture stability – is a hard task to overcome. Excellent device packaging technology without damaging the PSC performance is in need. This opportunity invites careful investigation of the perovskite material and device interface properties, and also new encapsulation materials and technologies. Meanwhile, it is also necessary to change the active layer fundamentally. Increasing the formation energy and tolerance factor through partial doping or alloying of the perovskite with various metal ions will improve both the thermal- and phase-stability. The more stable crystal structure will allow the perovskite to tolerate poorer conditions.

An exciting frontier in CsPbI₂Br PSCs is to integrate of these devices as the front cell in tandem photovoltaics, with the goal of creating high-efficiency solar cells through maximize the spectral capture efficiency. Toward enhancing light utilization in the photo-active layers, light trapping designs including geometric- and plasmonic-design without physically increasing the perovskite film thickness can be adopted. The transparent multilayer electrode between the front and the back cells needs to be optimized in order to provide a progression of work functions.

The past 2 years witness the development of CsPbI₂Br PSCs – for both experimental studies and theoretical calculations. Usual methods – including crystallization control, surface passivation, interface engineering, and device structure design – have been employed to improve the device performance. Is there anything beyond? The recent success in colloidal QD solids gives us inspiration. Just like a crystal is an ordered arrangement of atoms, a QD solid consists of an ordered distribution of QDs. The electron mobilities of QD solids can be larger than 10 cm² Vs⁻¹,^[68] which is similar to that of high-mobility crystals, leading to record-breaking performance in QD solar cells. Thus, PSCs employing CsPbI₂Br QD solids may be promising for next generation perovskite photovoltaics, taking advantage of the outstanding properties of both bulk films and QDs.

Acknowledgements

Q.Z. and X.Z. contributed equally to this work. This work was financially supported by the National Science Foundation of China (NSFC) under Grant Nos. 51433003 and 51702115, the National key research and development program of China (2016YFB0401701), the National Basic Research Program of China (973 Program) under Grant No. 2014CB643503, National Postdoctoral Program for Innovative Talents (BX201600060), China Postdoctoral Science Foundation Funded Project (2017M611319), JLU Science and Technology Innovative Research Team 2017TD-06, and the Opening funds of State Key Laboratory of Applied Optics, Changchun Institute of

Optics, Fine Mechanics and Physics, Chinese Academy of Science.

Conflict of Interest

The authors declare no conflict of interest.

Keywords

absorption coefficient, CsPbI₂Br, inorganic perovskites, solar cells, theoretical PCE

Received: August 31, 2018

Revised: September 29, 2018

Published online: October 30, 2018

- [1] Z. Chen, Q. Dong, Y. Liu, C. Bao, Y. Fang, Y. Lin, S. Tang, Q. Wang, X. Xiao, Y. Bai, Y. Deng, J. Huang, *Nat. Commun.* **2017**, *8*, 1890.
- [2] H. Wei, Y. Fang, P. Mulligan, W. Chuirazzi, H.-H. Fang, C. Wang, B. R. Ecker, Y. Gao, M. A. Loi, L. Cao, J. Huang, *Nat. Photon.* **2016**, *10*, 333.
- [3] H. Wei, D. DeSantis, W. Wei, Y. Deng, D. Guo, T. J. Savenije, L. Cao, J. Huang, *Nat. Mater.* **2017**, *16*, 826.
- [4] Z.-K. Wang, M. Li, Y.-G. Yang, Y. Hu, H. Ma, X.-Y. Gao, L.-S. Liao, *Adv. Mater.* **2016**, *28*, 6695.
- [5] NREL, <https://www.nrel.gov/pv/assets/images/efficiency-chart-20180716.jpg>. **2018**, Accessed: Aug 2018.
- [6] A. Kojima, K. Teshima, Y. Shirai, T. Miyasaka, *J. Am. Chem. Soc.* **2009**, *131*, 6050.
- [7] a) N. Li, Z. Zhu, J. Li, A. K. Y. Jen, L. Wang, *Adv. Energy Mater.* **2018**, *8*, 1800525. b) W. Travis, E. N. K. Glover, H. Bronstein, D. O. Scanlon, R. G. Palgrave, *Chem. Sci.* **2016**, *7*, 4548.
- [8] a) H. Jiang, J. Feng, H. Zhao, G. Li, G. Yin, Y. Han, F. Yan, Z. Liu, S. (Frank) Liu, *Adv. Sci.* **2018**, 1801117; b) J. S. Niezgodna, B. J. Foley, A. Z. Chen, J. J. Choi, *ACS Energy Lett.* **2017**, *2*, 1043; c) W. Ahmad, J. Khan, G. Niu, J. Tang, *Solar RRL* **2017**, *1*, 1700048; d) J. Liang, J. Liu, Z. Jin, *Solar RRL* **2017**, *1*, 1700086; e) C. Dong, X. Han, Y. Zhao, J. Li, L. Chang, W. Zhao, *Solar RRL* **2018**, 1800139; f) Q. Ma, S. Huang, X. Wen, M. A. Green, A. W. Y. Ho-PL Baillie, *Adv. Energy Mater.* **2016**, *6*, 1502202; g) J. Liang, P. Zhao, C. Wang, Y. Wang, Y. Hu, G. Zhu, L. Ma, J. Liu, Z. Jin, *J. Am. Chem. Soc.* **2017**, *139*, 14009; h) H. Chen, S. Xiang, W. Li, H. Liu, L. Zhu, S. Yang, *Solar RRL* **2018**, *2*, 1700188; i) S. Xiang, Z. Fu, W. Li, Y. Wei, J. Liu, H. Liu, L. Zhu, R. Zhang, H. Chen, *ACS Energy Lett.* **2018**, *3*, 1824–1831; j) Y. Li, Y. Wang, T. Zhang, S. Yoriya, P. Kumnorkaew, S. Chen, X. Guo, Y. Zhao, *Chem. Commun.* **2018**, *54*, 9809.
- [9] H. Choi, J. Jeong, H.-B. Kim, S. Kim, B. Walker, G.-H. Kim, J. Y. Kim, *Nano Energy* **2014**, *7*, 80.
- [10] G. E. Eperon, G. M. Paternò, R. J. Sutton, A. Zampetti, A. A. Haghighirad, F. Cacialli, H. J. Snaith, *J. Mater. Chem. A* **2015**, *3*, 19688.
- [11] A. Swarnkar, A. R. Marshall, E. M. Sanehira, B. D. Chernomordik, D. T. Moore, J. A. Christians, T. Chakrabarti, J. M. Luther, *Science* **2016**, *354*, 92.
- [12] Y. Hu, F. Bai, X. Liu, Q. Ji, X. Miao, T. Qiu, S. Zhang, *ACS Energy Lett.* **2017**, *2*, 2219.
- [13] a) Q. Wang, X. Zheng, Y. Deng, J. Zhao, Z. Chen, J. Huang, *Joule* **2017**, *1*, 371; b) Y. Fu, M. T. Rea, J. Chen, D. J. Morrow, M. P. Hautzinger, Y. Zhao, D. Pan, L. H. Manger, J. C. Wright, R. H. Goldsmith, S. Jin, *Chem. Mater.* **2017**, *29*, 8385; c) B. Li,

- Y. Zhang, L. Fu, T. Yu, S. Zhou, L. Zhang, L. Yin, *Nat. Commun.* **2018**, *9*, 1076;
- [14] a) T. Zhang, M. I. Dar, G. Li, F. Xu, N. Guo, M. Grätzel, Y. Zhao, *Sci. Adv.* **2017**, *3*, e1700841; b) Y. Jiang, J. Yuan, Y. Ni, J. Yang, Y. Wang, T. Jiu, M. Yuan, J. Chen, *Joule* **2018**, *2*, 1356;
- [15] a) E. M. Sanehira, A. R. Marshall, J. A. Christians, S. P. Harvey, P. N. Ciesielski, L. M. Wheeler, P. Schulz, L. Y. Lin, M. C. Beard, J. M. Luther, *Sci. Adv.* **2017**, *3*, eaao4204; b) Q. Wang, Z. Jin, D. Chen, D. Bai, H. Bian, J. Sun, G. Zhu, G. Wang, S. F. Liu, *Adv. Energy Mater.* **2018**, *8*, 1800007; c) Y. Wang, T. Zhang, M. Kan, Y. Li, T. Wang, Y. Zhao, *Joule* **2018**, *2*, 2065.
- [16] R. J. Sutton, G. E. Eperon, L. Miranda, E. S. Parrott, B. A. Kamino, J. B. Patel, M. T. Hörantner, M. B. Johnston, A. A. Haghighirad, D. T. Moore, H. J. Snaith, *Advanced Energy Materials* **2016**, *6*, 1502458.
- [17] a) D. Bai, H. Bian, Z. Jin, H. Wang, L. Meng, Q. Wang, S. Liu, *Nano Energy* **2018**, *52*, 408; b) L. Yan, Q. Xue, M. Liu, Z. Zhu, J. Tian, Z. Li, Z. Chen, Z. Chen, H. Yan, H. L. Yip, Y. Cao, *Adv. Mater.* **2018**, *30*, 1802509.
- [18] G. R. Berdiyrov, A. Kachmar, F. El-Mellouhi, M. A. Carignano, M. El-Amine Madjet, *J. Phys. Chem. C* **2016**, *120*, 16259.
- [19] Z. Yang, A. Surrente, K. Galkowski, A. Miyata, O. Portugall, R. J. Sutton, A. A. Haghighirad, H. J. Snaith, D. K. Maude, P. Plochocka, R. J. Nicholas, *ACS Energy Lett.* **2017**, *2*, 1621.
- [20] A. Miyata, A. Mitioglu, P. Plochocka, O. Portugall, J. T. -W. Wang, S. D. Stranks, H. J. Snaith, R. J. Nicholas, *Nat. Phys.* **2015**, *11*, 582.
- [21] C. L. Kennedy, A. H. Hill, E. S. Massaro, E. M. Grumstrup, *ACS Energy Lett.* **2017**, *2*, 1501.
- [22] J. S. Manser, P. V. Kamat, *Nat. Photon.* **2014**, *8*, 737.
- [23] A. H. Hill, K. E. Smyser, C. L. Kennedy, E. S. Massaro, E. M. Grumstrup, *J. Phys. Chem. Lett.* **2017**, *8*, 948.
- [24] a) C. Liu, W. Li, C. Zhang, Y. Ma, J. Fan, Y. Mai, *J. Am. Chem. Soc.* **2018**, *140*, 3825; b) S. Zhang, S. Wu, W. Chen, H. Zhu, Z. Xiong, Z. Yang, C. Chen, R. Chen, L. Han, W. Chen, *Mater. Today Energy* **2018**, *8*, 125; c) F. Yang, D. Hirotani, G. Kapil, M. A. Kamarudin, C. H. Ng, Y. Zhang, Q. Shen, S. Hayase, *Angew. Chem. Int. Ed.* **2018**, *57*, 12745.
- [25] J. Lin, M. Lai, L. Dou, C. S. Kley, H. Chen, F. Peng, J. Sun, D. Lu, S. A. Hawks, C. Xie, F. Cui, A. P. Alivisatos, D. T. Limmer, P. Yang, *Nat. Mater.* **2018**, *17*, 261.
- [26] A. Halder, D. Choudhury, S. Ghosh, A. S. Subbiah, S. K. Sarkar, *J. Phys. Chem. Lett.* **2015**, *6*, 3180.
- [27] L. Fu, Y. Zhang, B. Chang, B. Li, S. Zhou, L. Zhang, L. Yin, *J. Mater. Chem. A* **2018**, *6*, 13263.
- [28] Z. Zeng, J. Zhang, X. Gan, H. Sun, M. Shang, D. Hou, C. Lu, R. Chen, Y. Zhu, L. Han, *Adv. Energy Mater.* **2018**, *8*, 1801050.
- [29] J. K. Nam, M. S. Jung, S. U. Chai, Y. J. Choi, D. Kim, J. H. Park, *J. Phys. Chem. Lett.* **2017**, *8*, 2936.
- [30] a) C.-Y. Chen, H.-Y. Lin, K.-M. Chiang, W.-L. Tsai, Y.-C. Huang, C.-S. Tsao, H.-W. Lin, *Adv. Mater.* **2017**, *29*, 1605290; b) W. Zhou, Y. Zhao, X. Zhou, R. Fu, Q. Li, Y. Zhao, K. Liu, D. Yu, Q. Zhao, *J. Phys. Chem. Lett.* **2017**, *8*, 4122.
- [31] D. W. deQuilettes, W. Zhang, V. M. Burlakov, D. J. Graham, T. Leijtens, A. Osherov, V. Bulović, H. J. Snaith, D. S. Ginger, S. D. Stranks, *Nat. Commun.* **2016**, *7*, 11683.
- [32] D. J. Slotcavage, H. I. Karunadasa, M. D. McGehee, *ACS Energy Lett.* **2016**, *1*, 1199.
- [33] Z. Xiao, L. Zhao, N. L. Tran, Y. L. Lin, S. H. Silver, R. A. Kerner, N. Yao, A. Kahn, G. D. Scholes, B. P. Rand, *Nano Lett.* **2017**, *17*, 6863.
- [34] R. E. Beal, D. J. Slotcavage, T. Leijtens, A. R. Bowering, R. A. Belisle, W. H. Nguyen, G. F. Burkhard, E. T. Hoke, M. D. McGehee, *J. Phys. Chem. Lett.* **2016**, *7*, 746.
- [35] E. T. Hoke, D. J. Slotcavage, E. R. Dohner, A. R. Bowering, H. I. Karunadasa, M. D. McGehee, *Chem. Sci.* **2015**, *6*, 613.
- [36] Y.-C. Zhao, W.-K. Zhou, X. Zhou, K.-H. Liu, D.-P. Yu, Q. Zhao, *Light Sci. Appl.* **2016**, *6*, e16243.
- [37] R. Gottesman, L. Gouda, B. S. Kalanoor, E. Haltzi, S. Tirosh, E. Rosh-Hodesh, Y. Tischler, A. Zaban, C. Quarti, E. Mosconi, F. De Angelis, *J. Phys. Chem. Lett.* **2015**, *6*, 2332.
- [38] H. Zhu, K. Miyata, Y. Fu, J. Wang, P. P. Joshi, D. Niesner, K. W. Williams, S. Jin, X.-Y. Zhu, *Science* **2016**, *353*, 1409.
- [39] C. G. Bischak, C. L. Hetherington, H. Wu, S. Aloni, D. F. Ogletree, D. T. Limmer, N. S. Ginsberg, *Nano Lett.* **2017**, *17*, 1028.
- [40] J. Liang, C. Wang, Y. Wang, Z. Xu, Z. Lu, Y. Ma, H. Zhu, Y. Hu, C. Xiao, X. Yi, G. Zhu, H. Lv, L. Ma, T. Chen, Z. Tie, Z. Jin, J. Liu, *J. Am. Chem. Soc.* **2016**, *138*, 15829.
- [41] S. Mariotti, O. S. Hutter, L. J. Phillips, P. J. Yates, B. Kundu, K. Durose, *ACS Appl. Mater. Interfaces* **2018**, *10*, 3750.
- [42] C. F. J. Lau, M. Zhang, X. Deng, J. Zheng, J. Bing, Q. Ma, J. Kim, L. Hu, M. A. Green, S. Huang, A. Ho-Baillie, *ACS Energy Lett.* **2017**, *2*, 2319.
- [43] J.-W. Lee, H.-S. Kim, N.-G. Park, *Acc. Chem. Res.* **2016**, *49*, 311.
- [44] Y. Bai, S. Xiao, C. Hu, T. Zhang, X. Meng, Q. Li, Y. Yang, K. S. Wong, H. Chen, S. Yang, *Nano Energy* **2017**, *34*, 58.
- [45] L. Zhang, B. Li, J. Yuan, M. Wang, T. Shen, F. Huang, W. Wen, G. Cao, J. Tian, *J. Phys. Chem. Lett.* **2018**, *9*, 3646.
- [46] P. Wang, X. Zhang, Y. Zhou, Q. Jiang, Q. Ye, Z. Chu, X. Li, X. Yang, Z. Yin, J. You, *Nat. Commun.* **2018**, *9*, 2225.
- [47] D. Bai, J. Zhang, Z. Jin, H. Bian, K. Wang, H. Wang, L. Liang, Q. Wang, S. F. Liu, *ACS Energy Lett.* **2018**, *3*, 970.
- [48] G. Yin, H. Zhao, H. Jiang, S. Yuan, T. Niu, K. Zhao, Z. Liu, S. F. Liu, *Adv. Funct. Mater.* **2018**, 1803269.
- [49] Q. Dong, Y. Fang, Y. Shao, P. Mulligan, J. Qiu, L. Cao, J. Huang, *Science* **2015**, *347*, 967.
- [50] a) Y. Wu, C. Wei, X. Li, Y. Li, S. Qiu, W. Shen, B. Cai, Z. Sun, D. Yang, Z. Deng, H. Zeng, *ACS Energy Lett.* **2018**, 2030; b) H. Liu, Z. Wu, H. Gao, J. Shao, H. Zou, D. Yao, Y. Liu, H. Zhang, B. Yang, *ACS Appl. Mater. Interfaces* **2017**, *9*, 42919; c) X. Zhang, C. Sun, Y. Zhang, H. Wu, C. Ji, Y. Chuai, P. Wang, S. Wen, C. Zhang, W. W. Yu, *J. Phys. Chem. Lett.* **2016**, *7*, 4602; d) H. Liu, Z. Wu, J. Shao, D. Yao, H. Gao, Y. Liu, W. Yu, H. Zhang, B. Yang, *ACS nano* **2017**, *11*, 2239; e) X. Zhang, X. Bai, H. Wu, X. Zhang, C. Sun, Y. Zhang, W. Zhang, W. Zheng, W. W. Yu, A. L. Rogach, *Angew. Chem. Int. Ed.* **2018**, *57*, 1; f) H. Sun, Z. Yang, M. Wei, W. Sun, X. Li, S. Ye, Y. Zhao, H. Tan, E. L. Kynaston, T. B. Schon, H. Yan, Z. H. Lu, G. A. Ozin, E. H. Sargent, D. S. Seferos, *Adv. Mater.* **2017**, *29*, 1701153;
- [51] a) Q. Zeng, Z. Chen, Y. Zhao, X. Du, F. Liu, G. Jin, F. Dong, H. Zhang, B. Yang, *ACS Appl. Mater. Interfaces* **2015**, *7*, 23223; b) Q. Zeng, Z. Chen, F. Liu, G. Jin, X. Du, T. Ji, Y. Zhao, Y. Yue, H. Wang, D. Meng, T. Xie, H. Zhang, B. Yang, *Solar RRL* **2017**, *1*, 1600020; c) Z. Chen, X. Du, Q. Zeng, B. Yang, *Mater. Chem. Front.* **2017**, *1*, 1502; d) M. Liu, O. Voznyy, R. Sabatini, F. P. Garcia, de Arquer, R. Munir, A. H. Balawi, X. Lan, F. Fan, G. Walters, A. R. Kirmani, S. Hoogland, F. Laquai, A. Amassian, E. H. Sargent, *Nature Mater.* **2017**, *16*, 258; e) Q. Zeng, L. Hu, J. Cui, T. Feng, X. Du, G. Jin, F. Liu, T. Ji, F. Li, H. Zhang, B. Yang, *ACS Appl. Mater. Interfaces* **2017**, *9*, 31345.
- [52] Q. Zeng, X. Zhang, X. Feng, S. Lu, Z. Chen, X. Yong, S. A. T. Redfern, H. Wei, H. Wang, H. Shen, W. Zhang, W. Zheng, H. Zhang, J. S. Tse, B. Yang, *Adv. Mater.* **2018**, *30*, 1705393.
- [53] S. Christodoulou, F. Di Stasio, S. Pradhan, A. Stavrinadis, G. Konstantatos, *J. Phys. Chem. C* **2018**, *122*, 7621.
- [54] S. Draguta, O. Sharia, S. J. Yoon, M. C. Brennan, Y. V. Morozov, J. S. Manser, P. V. Kamat, W. F. Schneider, M. Kuno, *Nat. Commun.* **2017**, *8*, 200.
- [55] Q. Ma, S. Huang, S. Chen, M. Zhang, C. F. J. Lau, M. N. Lockrey, H. K. Mulmudi, Y. Shan, J. Yao, J. Zheng, X. Deng, K. Catchpole, M. A. Green, A. W. Y. Ho-Baillie, *J. Phys. Chem. C* **2017**, *121*, 19642.
- [56] Y. Wang, T. Zhang, F. Xu, Y. Li, Y. Zhao, *Solar RRL* **2018**, *2*, 1700180.

- [57] H. Rao, S. Ye, F. Gu, Z. Zhao, Z. Liu, Z. Bian, C. Huang, *Adv. Energy Mater.* **2018**, *8*, 1800758.
- [58] a) X. Zheng, B. Chen, J. Dai, Y. Fang, Y. Bai, Y. Lin, H. Wei, Xiao, C. Zeng, J. Huang, *Nat. Energy* **2017**, *2*, 17102; b) M. Li, Z. K. Wang, M. P. Zhuo, Y. Hu, K. H. Hu, Q. Q. Ye, S. M. Jain, Y. G. Yang, X. Y. Gao, L. S. Liao, *Adv. Mater.* **2018**, *30*, e1800258; c) T. Niu, J. Lu, R. Munir, J. Li, D. Barrit, X. Zhang, H. Hu, Z. Yang, A. Amassian, K. Zhao, S. F. Liu, *Adv. Mater.* **2018**, *30*, e1706576.
- [59] M. Abdi-Jalebi, Z. Andaji-Garmaroudi, S. Cacovich, C. Stavarakas, B. Philippe, J. M. Richter, M. Alsari, E. P. Booker, E. M. Hutter, A. J. Pearson, S. Lilliu, T. J. Savenije, H. Rensmo, G. Divitini, C. Ducati, R. H. Friend, S. D. Stranks, *Nature* **2018**, *555*, 497.
- [60] J. K. Nam, S. U. Chai, W. Cha, Y. J. Choi, W. Kim, M. S. Jung, J. Kwon, D. Kim, J. H. Park, *Nano Lett.* **2017**, *17*, 2028.
- [61] J. Yuan, L. Zhang, C. Bi, M. Wang, J. Tian, *Solar RRL* **2018**, *1800188*.
- [62] Q. Xue, Y. Bai, M. Liu, R. Xia, Z. Hu, Z. Chen, X.-F. Jiang, F. Huang, S. Yang, Y. Matsuo, H.-L. Yip, Y. Cao, *Adv. Energy Mater.* **2017**, *7*, 1602333.
- [63] J. Zhang, D. Bai, Z. Jin, H. Bian, K. Wang, J. Sun, Q. Wang, S. F. Liu, *Adv. Energy Mater.* **2018**, *8*, 1703246.
- [64] H. Bian, D. Bai, Z. Jin, K. Wang, L. Liang, H. Wang, J. Zhang, Q. Wang, S. Liu, *Joule* **2018**, *2*, 1500.
- [65] a) X. G. Zhao, J. H. Yang, Y. Fu, D. Yang, Q. Xu, L. Yu, S. H. Wei, L. Zhang, *J. Am. Chem. Soc.* **2017**, *139*, 2630; b) J. Heyd, G. E. Scuseria, M. Ernzerhof, *J. Chem. Phys.* **2003**, *118*, 8207.
- [66] M. Saliba, T. Matsui, K. Domanski, J.-Y. Seo, A. Ummadisingu, S. M. Zakeeruddin, J.-P. Correa-Baena, W. R. Tress, A. Abate, A. Hagfeldt, M. Grätzel; *Science* **2016**, *354*, 206.
- [67] X. Hu, X.-F. Jiang, X. Xing, L. Nian, X. Liu, R. Huang, K. Wang, H.-L. Yip, G. Zhou, *Solar RRL* **2018**, *2*, 1800083.
- [68] G. R. Yettapu, D. Talukdar, S. Sarkar, A. Swarnkar, A. Nag, P. Ghosh, P. Mandal, *Nano Lett.* **2016**, *16*, 4838.